Experiments in Fluids (2025) 66:88
https://doi.org/10.1007/s00348-025-03994-2

RESEARCH ARTICLE

Influence of backward-facing steps on laminar-turbulent transition in two-dimensional boundary layers at subsonic Mach numbers

Steffen Risius[1,2] · **Marco Costantini**[1]

Received: 25 July 2024 / Revised: 20 December 2024 / Accepted: 3 February 2025

Abstract

Backward-facing steps (BFS) can have a detrimental impact on laminar flow lengths because of their strong effect on boundary layer transition. BFS with normalized step heights in the range of $h/\delta_1 \approx 0.1$ to 0.6 (corresponding to height-based Reynolds numbers of $\mathrm{Re}_h = (U_\infty h/\nu) \approx 230$ to 2430) were installed in a two-dimensional wind tunnel model and tested in the Cryogenic Ludwieg-Tube Göttingen, a blow-down wind tunnel with good flow quality. The influence of BFS on the location of laminar-turbulent transition was investigated over a wide range of unit Reynolds numbers from $\mathrm{Re}_1 = 17.5 \times 10^6\ \mathrm{m}^{-1}$ to $80 \times 10^6\ \mathrm{m}^{-1}$, three Mach numbers, $M = 0.35$, 0.50 and 0.65, and various streamwise pressure gradients. The measurement of the transition locations was accomplished non-intrusively by means of temperature-sensitive paint. Transition Reynolds numbers, calculated with the flow length up to the location of laminar-turbulent transition x_T, ranged from $\mathrm{Re}_{\mathrm{tr}} \approx 1 \times 10^6$ to 11×10^6, and were measured as a function of step height, pressure gradient, Reynolds and Mach numbers. Incompressible linear stability analysis was used to calculate amplification rates of Tollmien–Schlichting waves; transition N-factors were determined by correlation with the measured transition locations. In parallel to earlier investigations with a similar setup, this systematic approach was used to identify functional relations between non-dimensional step parameters (h/δ_1 and Re_h) and the relative change of the transition location. Furthermore, the change of the transition N-factor ΔN due to the installation of the steps was investigated. It was found that the installation of backward-facing steps with $h/\delta_1 \lesssim 0.15$ and $\mathrm{Re}_h \lesssim 300$ does not lead to a reduction of $\mathrm{Re}_{\mathrm{tr}}$ and to $\Delta N > 0$. However, increasing the step size results in a decreasing laminar flow length and thus an increasing ΔN. The reported results are in general agreement with earlier investigations at significantly lower Mach and Reynolds numbers.

1 Introduction

Natural laminar flow technology (NLF) is a promising way to reduce aircraft drag (Schrauf 2005). Furthermore, the correct prediction of laminar-turbulent transition also receives increasing attention from wind turbine manufacturers as the lift-to-drag ratio has a strong influence on the aerodynamic performance of wind turbine rotor blades (Özçakmak et al. 2020). However, small surface imperfections, such as steps and gaps, can reduce laminar flow lengths significantly, which makes it indispensable to define manufacturing tolerances for NLF airfoils (Nenni and Gluyas 1966; Holmes et al. 1985; Arnal 1992; Masad and Nayfeh 1993; Drake et al. 2010; Schrauf 2018). The impact of gaps on boundary layer stability and transition has been studied in Zahn and Rist (2015); Beguet et al. (2017); Crouch et al. (2022); Risius et al. (2023), among others. The influence of steps on laminar flow lengths has been examined in various publications (see, e.g., Perraud and Séraudie (2000); Wang and Gaster (2005); Edelmann and Rist (2015); Tufts et al. (2017); Crouch and Kosorygin (2020); Rius-Vidales and Kotsonis (2021); Costantini et al. (2022)); however, a systematic investigation on the influence of backward-facing steps (BFS) in two-dimensional boundary layers over a wide range of Mach and Reynolds numbers with varying pressure gradients has not been conducted, as discussed in Sect. 1.1. This type of investigation has been performed in the present work, which is based on earlier studies conducted with the same wind tunnel model inside the same test facility (Risius

✉ Steffen Risius
steffen.risius@dlr.de

[1] Institute of Aerodynamics and Flow Technology, German Aerospace Center (DLR), Bunsenstraße 10, 37073 Göttingen, Germany

[2] Department of Mechanical Engineering, Kiel University of Applied Sciences (FH Kiel), Grenzstraße 3, 24149 Kiel, Germany

Published online: 09 April 2025

et al. 2018a, 2023). The following description of materials and methods (Sect. 2) and the analysis of the transition Reynolds number is therefore kept as short as possible and is partially identical to the above mentioned publications where the interested reader may find more detailed information.

1.1 Motivation and features of the current study

Nenni and Gluyas (1966) were the first to study the influence of backward-facing steps on laminar-turbulent transition. They identified the Reynolds number, Re_h, calculated with the step height h, as most relevant parameter for the impact of BFS on transition. According to their findings, transition in the presence of a backward-facing step occurs earlier than on a smooth surface at a 'critical' step-height Reynolds number of $\mathrm{Re}_h = U_\infty \cdot h/\nu_\infty \approx 900$. This critical value of the step-height Reynolds number was recently confirmed in Schrauf (2018), although the different definitions of the Re_h (with the flow velocity U_e and flow viscosity ν_e at the boundary layer edge instead of U_∞ and ν_∞) and the different experimental configurations have to be considered.[1] Furthermore, these early studies aimed to identify an allowable tolerance for the height of steps (based on the critical Re_h), rather than analyzing the behavior of boundary layer transition for varying step-height Reynolds numbers.

The present work focuses on the effect of sharp-edged (Costantini et al. 2018) BFS on laminar-turbulent transition of two-dimensional boundary layers in a low-disturbance environment, in which Tollmien–Schlichting (T-S) waves are the dominant instability mechanism leading to transition. This flow configuration has been examined in Perraud and Séraudie (2000); Wang and Gaster (2005); Crouch et al. (2006); Drake et al. (2010); Schröder et al. (2013); Rizzetta and Visbal (2013); Crouch and Kosorygin (2020); Hildebrand et al. (2020); Franco et al. (2021); Tocci et al. (2022); Heintz and Scholz (2023). The influence of backward-facing steps on transition of boundary layers over swept wings and swept flat plates with predominant crossflow instabilities has been considered in Holmes et al. (1985); Perraud and Séraudie (2000); Duncan et al. (2013); Tufts et al. (2017); Eppink et al. (2018). Rounded BFS have been studied in Ragab et al. (1989); Masad and Nayfeh (1993); Franco and Hein (2022), whereas a backward-facing ramp was investigated in Holmes et al. (1985). The combination of the effect of wall suction and BFS has been examined in Hahn and Pfenninger (1973); Dimond et al. (2021) for sharp steps, and in Al-Maaitah et al. (1990) for rounded steps; the combination of the influence of wall cooling and a rounded BFS has been studied in Al-Maaitah et al. (1990).

Among earlier publications investigating boundary layers with predominant T-S instabilities, Perraud and Séraudie (2000); Wang and Gaster (2005); Crouch et al. (2006); Crouch and Kosorygin (2020); Heintz and Scholz (2023) have reported an experimental analysis of the impact of sharp BFS on transition complemented by boundary layer stability computations. The effect of the BFS was established in terms of the variation of the transition location x_T as a function of the step-height Reynolds number Re_h and/or of the relative step height h/δ_1, i.e., the step height normalized by the boundary layer displacement thickness at the step location, but in the absence of the step. The experimental data were also used to develop models for the prediction of the BFS influence on transition. These models rely on linear stability theory to compute the amplification factors (N-factors) of T-S waves and provide an estimation of the impact of the step as an additional T-S wave amplification (ΔN), which is obtained via correlation between the results of the boundary layer stability computations and the experimental data. A similar approach was followed by Hildebrand et al. (2020) on the basis of the experimental data reported in Wang and Gaster (2005).

The aforementioned experimental studies considered BFS in low-speed flows ($M < 0.3$) at relatively small unit Reynolds numbers ($\mathrm{Re}_1 = U_\infty/\nu_\infty < 5 \times 10^6\ \mathrm{m}^{-1}$). Moreover, most earlier work examined flat-plate configurations at (almost) zero pressure gradient, except for Perraud and Séraudie (2000); Crouch et al. (2006); Drake et al. (2010); Crouch and Kosorygin (2020); in these latter investigations, however, only two different streamwise pressure gradients were considered.

Mach and Reynolds numbers larger than those considered in previous work, and a range of streamwise pressure gradients are examined in the present experimental investigation on the impact of sharp-edged BFS on boundary layer transition. The influence of step height on the transition location is systematically investigated for four different step heights, three different subsonic Mach numbers ($M = 0.35, 0.50$ and 0.65), eight unit Reynolds numbers in the range of $\mathrm{Re}_1 = 17.5 \times 10^6\ \mathrm{m}^{-1}$ to $80 \times 10^6\ \mathrm{m}^{-1}$ and different streamwise pressure gradients. The study focuses on favorable pressure gradients, which are the most relevant for NLF surfaces. Nevertheless, also zero and adverse pressure gradients are examined. The nominal heights of the BFS are $h = 10\,\mu\mathrm{m}$, $20\,\mu\mathrm{m}$, $30\,\mu\mathrm{m}$ and $40\,\mu\mathrm{m}$. The boundary layer thickness at the step location in the absence of the step varies between $\delta_1 \approx 50\,\mu\mathrm{m}$ and $120\,\mu\mathrm{m}$. That results in normalized step heights that vary between $h/\delta_1 \approx 0.1$ to 0.6, which correspond to a height based Reynolds numbers in the range of $\mathrm{Re}_h = (U_\infty h/\nu) \approx 230$ to 2430, as shown in detail in Table 1.

[1] Transition is less sensitive to the impact of forward-facing steps (FFS), for which a critical Reynolds number $\mathrm{Re}_h \approx 1800$ was reported (Nenni and Gluyas 1966).

Table 1 Characteristic parameters of the investigated BFS in this study

Nominal	10 µm	20 µm	30 µm	40 µm
Real h	10.1 µm	21.6 µm	30.3 µm	38.6 µm
$h/\delta_1 \approx$	0.10–0.20	0.20–0.42	0.25–0.60	0.30–0.60
$\mathrm{Re}_h \approx$	227–811	487–1725	529–2431	679–1945

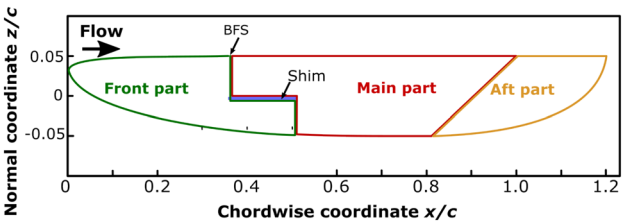

Fig. 1 Side view of the *PaLASTra* model with three parts. The step is located between the front and the main part at $x_S/c = 0.35$. The original chord length of $c = 0.2$ m is used for normalization of the chordwise coordinate, in line with previous work (Costantini et al. 2015b; Costantini 2016; Costantini et al. 2016, 2018; Risius et al. 2018b; Dimond et al. 2019, 2020, 2021)

The investigated step dimensions (in non-dimensional terms) are representative for the size of the steps that may occur on commercial transport aircraft wings and thus enable the transfer of the knowledge gained in fundamental research to applied aerodynamics. In the case of a single-aisle, mid-range subsonic transport aircraft, the mean aerodynamic chord length is about 4 m to 4.2 m (EASA 2017, 2023), which is about 20 times the chord length of the investigated wind tunnel model. Multiplication of the nominal step dimensions with a factor of 20 leads to a step height in the range of 0.2 mm to 0.8 mm at the wing of the aforementioned transport aircraft.

The systematic variation of flow parameters is based on the study of unit Reynolds numbers, Mach numbers and pressure gradients for the reference (smooth, i.e., step-free) surface reported by Risius et al. (2018b). Compared to earlier investigations on the influence of BFS on the transition location, this systematic approach allows a quantification of the effect of BFS in terms of the transition Reynolds number as a function of non-dimensional step parameters, pressure gradient parameters (characterized here by the incompressible shape factor) and the unit Reynolds number for different Mach numbers.

In parallel to Risius et al. (2018b, 2023), also boundary layer calculations and a linear stability analysis were performed on the basis of the pressure and temperature distributions measured on the investigated surface. The approach allowed to obtain the distributions of the amplification factors of T-S waves and thus the determination of the step-induced ΔN; this is accomplished via correlation of the computed N-factor distributions with the transition locations measured in the experiments with and without steps, as discussed in Sect. 2.5.

2 Materials and methods

The experiments were performed in the Cryogenic Ludwieg-Tube Göttingen (KRG), a blow-down wind tunnel operated intermittently with gaseous nitrogen as driving gas and good flow quality (Rosemann 1997; Koch 2004).

The wind tunnel model used for the present study was the two-dimensional *PaLASTra* model. The model is composed of three parts which are connected with the help of shims and bolts integrated into the model (see Fig. 1). This specific manufacturing of the model allows the installation of steps with high accuracy into the model between the front and the main part at $x_S/c = 0.35$ of the upper surface. During the first measurement campaigns, only the front and the main parts of the model were used, causing a large separation region behind the model, which results in strong pressure fluctuations that influence the measured transition locations (Costantini et al. 2015a; Costantini 2016; Costantini et al. 2016, 2018). In later measurement campaigns, the complete model including the aft-part was used, effectively reducing separation-induced pressure fluctuations (Risius et al. 2018a, b; Dimond et al. 2019, 2020, 2021; Risius et al. 2023).

In order to assure the correct installation of the BFS with minimal variation, the step height was measured systematically along the span with a profilometer. The standard deviation of the measured step height is in the range of 5 µm. As reported in Table 1, the nominal step height of 10 µm, 20 µm, 30 µm and 40 µm deviates slightly from the actual step height of 10.1 µm, 21.6 µm, 30.3 µm and 38.6 µm. The actual step heights are considered for the evaluation of the step-height parameters (h/δ_1, Re_h, etc.), while the nominal step heights are used throughout the article to refer to the different model configurations. The results from Franco and Hein (2022) indicate that small deviations from a perfectly sharp-edged BFS have a limited influence on the N-factor distribution for small step heights with $h/\delta_1 = 0.4$, which are the main focus of the current work. Furthermore, the deviation from the 'sharpness' studied in the current work is significantly less pronounced than the one investigated by Franco and Hein (2022) (see step contour in Costantini et al. (2018)). The BFS investigated here may therefore be realistically assumed as 'sharp-edged.'

2.1 Measurement of the pressure distribution

The model was equipped with a row of pressure taps to measure the surface pressure distribution (Costantini et al.

2015b; Costantini 2016; Costantini et al. 2018, 2016; Dimond et al. 2019; Risius et al. 2018a, 2023). Typical pressure distributions of the upper side of the modified *PaLASTra* model are shown in Fig. 2. The pressure gradient is essentially uniform over a large portion of the upper surface. Only around $x/c = 0.35$ the pressure coefficients show some slight variations from an ideally smooth distribution, which are due to the connection between the model parts and to the interfaces between different materials (Costantini et al. 2015b; Costantini 2016; Costantini et al. 2018; Risius et al. 2018b, 2023). At the same time, it can be observed in Fig. 2 that the pressure distributions of all step heights are almost identical to the pressure distributions of the reference configuration, provided that the flow conditions are reproduced. The steps had therefore no global effect on the pressure distributions. On the other hand, it should be emphasized here that the spatial resolution of the surface pressure measurements was not sufficient to measure the very strong, local pressure gradients occurring in close proximity of the BFS.

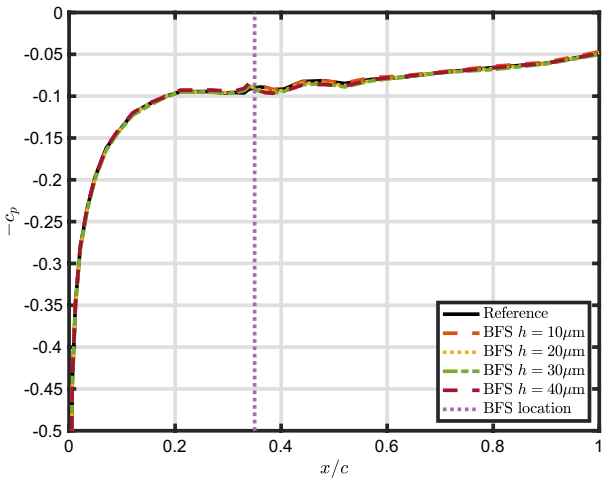

Fig. 2 Exemplary distribution of pressure coefficient, c_p, on model upper side at $\mathrm{Re}_1 = 22.5 \times 10^6\ \mathrm{m}^{-1}$, $M = 0.50$, $H_{12} \approx 2.58$ with an angle of attack of $-1.5°$

2.2 Measurement of the transition location

Boundary layer transition was measured, via an optical non-intrusive global measurement of the surface temperature distribution using a Temperature-Sensitive Paint (TSP) applied on the model upper surface (Liu et al. 2021). TSP formulation, surface quality, acquisition and evaluation of the TSP images were described in Ondrus et al. (2015); Costantini et al. (2018); Risius (2018); Risius et al. (2023), where further details can be found.

The series of TSP results shown in Fig. 3 was obtained for different step heights. The result image of the reference configuration can be seen on the very left of the series in Fig. 3. In this case, the transition location is closer to the trailing edge (with $x_T/c = 88.7\%$) and it moves upstream in four TSP images on the right with increasing step height. However, the transition locations for $h = 10\,\mu\mathrm{m}$ (with $x_T/c = 88.8\%$) and the reference configuration (with $x_T/c = 88.7\%$) are identical under consideration of the measurement uncertainties. The same observation of a negligible influence of the small step height of $h = 10\,\mu\mathrm{m}$ is common to many examined flow conditions and will be discussed later in this work.

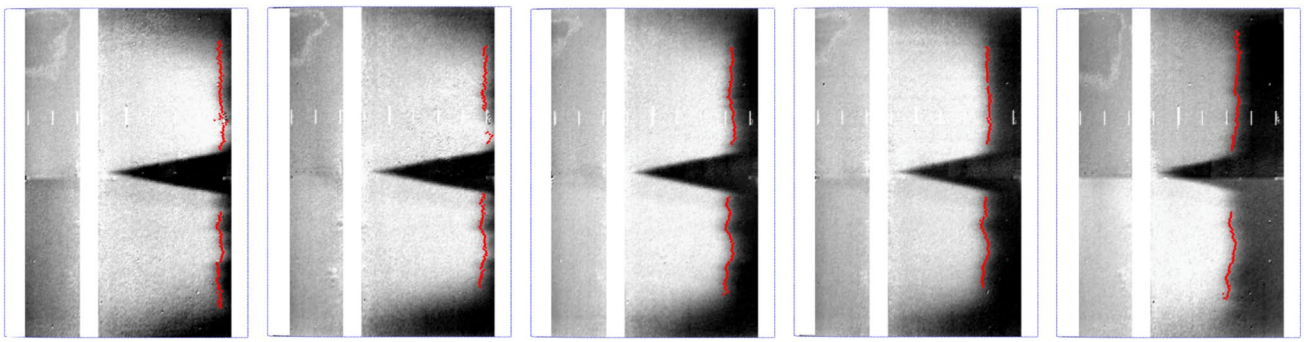

Fig. 3 TSP results on model upper side for five configurations with $h = 0$ µm, 10 µm, 20 µm, 30 µm and 40 µm (from left to right). The flow direction is from left to right, and the flow conditions are the same as in Figs. 2 and 6. The red dots indicate the detected transition locations by the maximal gradient technique at the undisturbed flow locations for each spanwise location (Costantini et al. 2021). The measured transition locations are $x_T/c = 88.7\%$, 88.8%, 81.8%, 79.1% and 72.9% (from left to right). The whitened strips indicate metallic surfaces of the model where no TSP had been applied or locations where optical artifacts prohibited the detection of the transition location. Markers indicating every 10% chord are visualized by thin white lines on the starboard side. Some contrast differences between the upper and lower half of the images are due to the measurement setup described in Risius (2018)

2.3 Analysis of the transition Reynolds number

The influences of pressure gradient and unit Reynolds number on transition Reynolds number $\mathrm{Re}_{tr} = x_T \cdot \mathrm{Re}_1$ are analyzed separately for each investigated Mach number: $M = 0.35$, 0.50 and 0.65. Detailed results will be presented here for $M = 0.5$ and $\mathrm{Re}_1 = 22.5 \times 10^6\ \mathrm{m}^{-1}$, while data from the other flow conditions are presented in Appendix. For better readability, unit Reynolds numbers and transition Reynolds numbers are normalized via $\mathrm{Re}_1^* = \mathrm{Re}_1/(10^6\ \mathrm{m})$ and $\mathrm{Re}_{tr}^* = \mathrm{Re}_{tr}/10^6$, respectively.

In parallel to the analysis of the reference configuration (Risius et al. 2018b) and the configuration with gaps (Risius et al. 2023), the same analysis was carried out for the modified *PaLASTra* model with installed backward-facing steps. The fitted linear approximation of the transition Reynolds number as a function of H_{12} is shown as solid lines in Fig. 4 for the considered case at $M = 0.5$ and $\mathrm{Re}_1^* = 22.5$, while the middle figures in Appendix (Figs. 15, 18, 21, 24, 27, 30, 33, 36, 39, 42, 45, 48, 51) report the results for the other flow conditions examined in this work. The black dashed lines show the averaged result of the reference configurations. The purple dotted line marks the Reynolds number corresponding to the location of the step at $x_S/c = 0.35$ with $\mathrm{Re}_{x_S} = x_S \cdot \mathrm{Re}_1$.

It can be seen that the transition occurs in most analyzed cases between the step and the transition location measured with the reference configuration. However, in agreement with the observations in Fig. 3, a BFS with $h = 10\,\mu\mathrm{m}$ leads to no reduction of transition location. That results in a similar Re_{tr}^* of the reference configuration and a BFS with $h = 10\,\mu\mathrm{m}$, which is about the symbol size. In agreement with Fig. 3, also Fig. 4 shows that backward-facing steps with $h > 10\,\mu\mathrm{m}$ result in a decreasing transition Reynolds number with step height compared to the reference configuration. These observations are consistent for all investigated Mach and Reynolds numbers, as shown in the middle figures in Appendix (Figs. 15, 18, 21, 24, 27, 30, 33, 36, 39, 42, 45, 48, 51). These results are also consistent with the data from Wang and Gaster (2005) as discussed later (Sect. 3.4).

In general, it was also found for the configuration with steps that an increasing unit Reynolds number leads to an increasing transition Reynolds number (Fig. 54 and Tables 3, 4, 5 and 6) and an increasing unit Reynolds number leads to a decreasing slope (Fig. 55 and Tables 7, 8, 9 and 10). These observations are presented in more detail in Appendix.

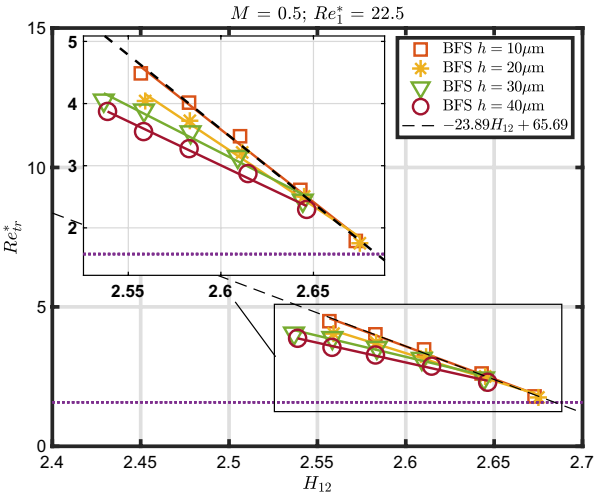

Fig. 4 Approximation of the influence of H_{12} on the transition Reynolds number for the configurations with steps. The fitted averaged function of the reference configuration is shown as dashed black line. The purple dotted line corresponds to the Reynolds number at the location of the step at $x_S/c = 0.35$. For better comparability, a zoomed area is shown in this figure as an inset

2.4 Boundary layer computations

Laminar boundary layer computations were performed using the compressible boundary layer solver COCO (Schrauf 1998), with a modification to incorporate the measured surface pressure and surface temperature distributions. COCO calculates a fully laminar boundary layer, which was used to determine incompressible displacement (δ_1) and momentum thickness (δ_2) of the laminar boundary layer. The average incompressible shape factor, $H_{12} = \delta_1/\delta_2$, was determined by averaging the incompressible shape factor curve between $24\% < x/c < 90\%$. The selection of the incompressible shape factor as pressure gradient parameter is motivated in Risius et al. (2018b). H_{12} can be also used to calculate other pressure gradient parameters, such as the Hartree parameter. In the present study, the Hartree parameter can be calculated by $\beta_H = -0.687 \cdot H_{12} + 1.810$ (Risius et al. 2018b). A smaller value of H_{12} corresponds to a stronger favorable pressure gradient and a larger β_H, leading to an accelerated boundary layer. Most data points in this study are in the range of $\beta_H \approx -0.05$ to 0.10, which leads to a significant movement of the transition location even in the presence of BFS. In the case of Fig. 4, a small change in H_{12} from 2.65 to 2.55 leads to almost a doubling of Re_{tr} for the smooth configuration, and to a significant increase in Re_{tr} also for the configuration with the highest step.

2.5 Stability analysis and the ΔN method

Tollmien–Schlichting (T-S) waves are the dominant instability mechanism leading to transition in two-dimensional boundary layers (Schlichting et al. 2006). Amplification factors of T-S waves for the computed boundary layer were determined by means of LILO (Schrauf 2006). The

amplification factor N is determined by the envelope strategy, which uses the most amplified T-S wave at each transition location. Based on the findings of Risius et al. (2018b), the incompressible N-factors are considered in the present analysis. According to linear, local stability theory and the quasi-parallel flow assumption, incompressible stability computations were carried out, and their results were correlated with the measured transition location to assess transition N-factors. The e^N method assumes that transition occurs when a transition N-factor N_{tr} is reached (van Ingen 1956; Smith and Gamberoni 1956). The transition N-factors N_{tr} are determined via correlation of the results of linear stability computations with experimental transition data. For each configuration, the transition location was measured with help of the TSP result. For the cases of Fig. 6, it is indicated by vertical lines. The intercept of the transition location with the maximal N-factor curve is used to determine the transition N-factor (the horizontal lines in Fig. 6). This procedure is carried out for each measurement point of each configuration and used for the analysis.

The ΔN method can be used to model the effect of steps (Wang and Gaster 2005; Crouch et al. 2006; Edelmann and Rist 2015; Costantini et al. 2022) and gaps (Beguet et al. 2017; Crouch 2022; Crouch et al. 2022) on boundary layer stability. As reported in those publications, the presence of steps or gaps leads to an additional amplification of the T-S waves resulting in an increase of the N-factor (ΔN) as compared to the N-factor distribution of the smooth surface, see, for example, Figs. 8 and 11 in Edelmann and Rist (2015). In contrast to the results cited above, the N-factor distributions in the current study (Fig. 6), in line the ones shown in Risius et al. (2023) for gaps, are very similar for the reference and the BFS configurations, which is accounted to the measured pressure distributions and resulting boundary layer calculations. In fact, as shown in Fig. 2 the pressure distributions measured for the different model configurations are essentially the same. Therefore, the present numerical simulations, based on the measured pressure distributions, miss the strong, localized disturbances induced by the step. The undulations after the step of the N-factor curve, visible in Fig. 6, are not caused by the step itself, but instead rather caused by slight surface variations due to the integration of the TSP layer into the pocket of the wind tunnel model (Sect. 2.1). In practice, the procedure to calculate ΔN becomes analogous to that presented in Wang and Gaster (2005), Crouch et al. (2006), Crouch (2022) and Crouch et al. (2022): As proposed in those publications, ΔN is obtained from the difference between the N-factors determined for the smooth and BFS configurations, see Fig. 6. Although it appears as a decrement in N_{tr}, it is indeed a model for the BFS-induced increment in disturbance amplification. According to this method, only the far-field change in the amplification factor ΔN, compared to the smooth surface, is linked to the potential movements of the transition location.

The transition N-factors are shown as a function of H_{12} for individual combinations of M and Re_1^* in Fig. 7 and in the bottom figures in Appendix (Figs. 16, 19, 22, 25, 28, 31, 34, 37, 40, 43, 46, 49, 52). The good repeatability of the results from different wind tunnel entries can be seen also by comparing the N-factor results of different reference configurations in these figures.

In agreement with the results for gaps (Risius et al. 2023), it was found that H_{12} has an appreciable influence on the transition N-factor for an accelerated boundary layer even in the presence of BFS. Only at larger values of the shape factor ($H_{12} \gtrsim 2.59$) corresponding to decelerated boundary layers, the transition N-factors were found to reach a plateau. The dependency of the transition N-factor on H_{12} was already mentioned by Arnal et al. (1997) for smooth surfaces and was accounted to shortcomings of the e^N-method as, for instance, nonparallel effects, the receptivity process or nonlinear mechanisms (Risius et al. 2018b).

The analysis of the different N-factor distributions shows that, despite the change of N as a function of H_{12} for $H_{12} \lesssim 2.59$, the step-induced ΔN remains essentially uniform, i.e., independent from H_{12}. Thus, a uniform $\Delta N = N_{\mathrm{reference}} - N_{\mathrm{step}}$ is assumed. In order to quantify the constant offset by ΔN, the determined slopes for all configurations were averaged and plotted for the approximated range of H_{12}: They are presented as solid lines with the colors of the corresponding datasets in the bottom figures in Appendix (Figs. 16, 19, 22, 25, 28, 31, 34, 37, 40, 43, 46, 49, 52).

In order to determine the reduction of the transition N-factor by installation of the step, a linear function is used to approximate the dependency of the incompressible transition N-factor on H_{12}. This approximation is carried out separately for each step height and for each flow condition, defined by the specific M and Re_1^*. For each dataset, the range of H_{12} used for the linear approximation was chosen separately depending on the distribution of the data points used, in a manner analogous to that reported in Risius et al. (2018b, 2023).

By comparing the offset between the linear approximations, the resulting ΔN, caused by the installation of the steps, are determined systematically and compared in Sect. 3.5. It should be noted here that the analysis of ΔN focuses on the favorable and zero pressure gradients, while adverse pressure gradients are not considered.

2.6 Relative change of the transition location and influence of the step height

The transition location can also be used to calculate the relative variation of the transition location by the ξ-parameter (see, for example, Perraud and Séraudie (2000) and

Costantini et al. (2015b) for the analysis of step effects, or Crouch et al. (2022); Risius et al. (2023) for the study of gaps). The ξ-parameter gives the distance from the step to the transition location, normalized by this distance in the absence of a step:

$$\xi = \frac{x_T - x_S}{x_{T0} - x_S} \tag{1}$$

The transition location in the absence of a step is given by x_{T0}, and in the presence of a step by x_T, while the location of the step is fixed at $x_S = 70\,\text{mm}$. For values of $\xi = 1$, the transition position is equivalent to that of the reference configuration, while for values $\xi = 0$, transition occurs directly at the step.

The evaluation of the relative change in transition location with respect to the step location, ξ, as a function of the non-dimensional step parameters, h/δ_1 and Re_h, enables to isolate the effect of the BFS on boundary layer transition from the influence of the other factors, in a manner analogous to that discussed for forward-facing steps in Costantini (2016) and Costantini et al. (2022). As summarized in Costantini (2016), a similar behavior was reported also for two-dimensional roughness in the form of cylindrical wires placed perpendicular to the incoming flow (Dryden 1953; Tani 1961).

3 Results and discussion

3.1 The unit Reynolds number effect

As described above (Sect. 2.3), the transition Reynolds number increases with increasing unit Reynolds number. This observation is known as 'unit Reynolds number effect' and has been investigated and discussed in detail in Risius et al. (2018b). It is known that a power relation exists with $\mathrm{Re}^*_{\mathrm{tr}} \sim \left(\mathrm{Re}^*_1\right)^{\alpha_{III}}$. The exponents of the results presented here can be found by estimating the slopes of $\log(\mathrm{Re}^*_{\mathrm{tr}})$ against $\log(\mathrm{Re}_1)$ as done, for example, for $H_{12} = 2.55$ in Fig. 8. The exponent α_{III} was found to vary between approximately 0.4 and 0.7. It is therefore in agreement with earlier findings, which are in the same range (Arnal 1989; Risius et al. 2018b, 2023). It should be stressed here that the investigated Reynolds number range between $\mathrm{Re}_1 = 17.5 \times 10^6$ and 80×10^6 is significantly larger than those examined in previous studies on the influence of BFS, where $\mathrm{Re}_1 < 5 \times 10^6$, as discussed in Sect. 1. It is the first time that the effect of the variation of such a high Reynolds number on BFS-induced transition has been investigated.

On the other hand, ξ and the transition N-factor for the BFS configurations did not present a clear dependency on Re_1. (The corresponding plots are therefore not shown.) This result is also in agreement with the observations reported in Costantini (2016); Costantini et al. (2022) for FFS configurations and in Risius et al. (2023) for gap configurations.

3.2 Mach number influence

A comparison of the different Mach numbers (data points with same color and different symbols in Figs. 8 and 56) shows that even though the Mach number appears to have an influence (increase in $\mathrm{Re}^*_{\mathrm{tr}}$ with decreasing M), this effect remains within the measurement uncertainty for the investigated configurations, in agreement with the results reported earlier for reference (Risius et al. 2018b) and gap configurations (Risius et al. 2023). It should be remarked here that a variation of the Mach number in KRG also leads to a change in the disturbance environment and in the model surface temperature ratio (wall temperature/adiabatic-wall temperature). An exclusive analysis of Mach number effects can be carried out when disturbance levels of the wind tunnel and the wall temperature ratio are taken into account and their influence is corrected, as discussed in Risius et al. (2018b). In the current study, as in Risius et al. (2023), this kind of systematic correction has not been conducted, as it requires a large number of data points for each model configuration and a detailed knowledge of the disturbance environment. The latter would require details on the receptivity process in the presence of steps, which are unknown and will result in further uncertainties. Nevertheless, the evaluation of the experimental results as ξ vs. h/δ_1 and Re_h did enable the isolation of the influence of BFS on boundary layer transition from the Mach number effect, as can be seen in Figs. 9 and 10.

It should be noted that the current study is also the first systematic investigation of the Mach number influence on BFS-induced transition. For FFS configurations, the Mach number was also found to have no appreciable effect on the relation between ξ and the non-dimensional step parameters h/δ_1 and Re_h (Costantini 2016; Costantini et al. 2022).

3.3 Influence of the shape factor H_{12} on the ξ-parameter

When the experimental results are investigated by ξ as a function of the non-dimensional step parameters, the impact of the pressure gradient is essentially incorporated into the relative change in transition location, since both x_T and x_{T0} vary with the pressure gradient. In this manner, the relation between ξ and h/δ_1 as well as Re_h was shown to be practically independent of H_{12}, as can be seen in Figs. 9 and 10 and in Table 2. This result is analogous to the findings for FFS reported in Costantini et al. (2015b, 2016); Costantini (2016); Costantini et al. (2018, 2022) and for cylindrical wires reported in Dryden (1953); Tani (1961). The analysis of various investigations

conducted in Smith and Clutter (1959) generally concluded that 'pressure distribution effects are of minor importance in determining critical roughness.' However, this may hold only when the pressure gradient is changed while remaining uniform in the examined region. For the airfoil investigated in Perraud and Séraudie (2000), a change of the angle of attack from $AoA = -6°$ to $-1°$ led to a reduction of the critical step height, probably because of the change of the pressure gradients in the region where transition occurred. (x_T and x_{T0} may be located in regions with different pressure gradients.) A similar aspect should be considered for the evaluation of the two pressure gradients (implemented by using two different models) examined in Drake et al. (2010): In particular, for the model with the moderately favorable pressure gradient, the steps were indeed mounted at a location immediately downstream of a region of adverse pressure gradient. Thus, the pressure gradient was not uniform in the investigated region ($x_{T0} - x_S$).

3.4 Influence of the step height on the ξ-parameter

In Fig. 9, the ξ-parameter is plotted as a function of the normalized step height, h/δ_1. It can be seen that a relative increase in step height compared to boundary layer thickness h/δ_1 leads to a larger reduction of ξ, as expected by the results presented in the previous sections. The influence of the BFS generally increases with step height from $h = 10\,\mu$m (orange), $h = 20\,\mu$m (yellow), $h = 30\,\mu$m (green) to $h = 40\,\mu$m (dark-red). The observed trend can be approximated with a linear function as $\xi = m \cdot \frac{h}{\delta_1} + b$, with the slope m and the intercept b. The approximation is shown as a black line in Fig. 9, and the values for m and b are summarized in Table 2 for different shape factors. The same analysis has been conducted for ξ as a function of Re_h which is shown in Fig. 10. Both representations of the results provided good correlations of the experimental data, except for a few outliers, which are likely due to the limited amount of data at large Reynolds numbers. Data from earlier work are also shown in Figs. 9 and 10, as discussed below.

It should be noted in these figures that values of ξ even larger than 1 were found at small h/δ_1 and Re_h. This observation, however, should not be misinterpreted as a favorable effect of small BFS (increasing laminar flow length as compared to the reference configuration). In the current study, the corresponding values of ξ are within the measurement accuracy and are likely accounted to small differences in the model setup inside the wind tunnel for different step configurations. Since the measurements were conducted over a time span of two years at six different wind tunnel entries, it may be related to the resulting small variations of the flow conditions. Furthermore, a strictly linear function may not represent appropriately the results for the whole range of examined non-dimensional step parameters. For practical applications, a condition of $\xi = 1$ for $h/\delta_1 = 0$ and $\mathrm{Re}_h = 0$ would provide a more suitable approximation of the present data.

The quantitative relations identified in the current work are compared in Figs. 9 and 10 with the data (Wang and Gaster 2005; Hildebrand et al. 2020; Crouch et al. 2006) and criteria (Nenni and Gluyas 1966) reported in the literature. (The data from Perraud and Séraudie (2000) are not shown in the figures because of their variation in the streamwise pressure gradient (see Sect. 3.3), but for the case at $AoA = -1°$ the trends would be similar to those of Wang and Gaster (2005).) A gradual reduction in ξ was found in the present work for increasing h/δ_1 and Re_h, in qualitative agreement with earlier work (Perraud and Séraudie 2000; Wang and Gaster 2005; Hildebrand et al. 2020). As described above, an appreciable impact of the BFS was observed only above a certain step height, i.e., at approximately $h/\delta_1 > 0.17$ and at $\mathrm{Re}_h > 270$. The critical value of h/δ_1 was higher in Wang and Gaster (2005) than in the present work, and higher values of ξ were also reported in that work for the same values of h/δ_1 (see Fig. 9). The data from Crouch et al. (2006) show significant scatter, but appear to range between the current results and those from Wang and Gaster (2005). On the other hand, the present results are quantitatively in agreement with those from Wang and Gaster (2005) up to $\mathrm{Re}_h \approx 800$ (with $\xi \approx 0.8$), whereas the data from Hildebrand et al. (2020) showed slightly lower values of both datasets. For $\mathrm{Re}_h > 800$, higher values of ξ were generally measured in the present work, as compared to Wang and Gaster (2005) (see Fig. 10). Analogous observations hold also for the comparison with the results from Perraud and Séraudie (2000); Hildebrand et al. (2020). The observed differences may be due to the different ranges of examined Mach and unit Reynolds numbers, to differences in the disturbance environment, to variations in the pressure distribution in the region between x_S and x_{TO}, and to the actual geometry of the investigated BFS (see Costantini (2016) for a detailed discussion with regard to FFS). Dedicated experiments would be needed to clarify the main reason for the differences in the ξ-values.

At this point, it should be emphasized that the step-height Reynolds number was confirmed as an appropriate parameter for the description of the step impact on transition and for the comparison of different investigations, in spite of the information about the step location and the local boundary layer state not contained in Re_h. This finding is in line with other work (see, e.g., Schrauf (2018); Costantini (2016); Costantini et al. (2022); Hildebrand et al. (2020)).

In this context, it is also interesting to note that the fit to the data from Wang and Gaster (2005) reported in Hildebrand et al. (2020) also results in a ξ larger than 1 at small

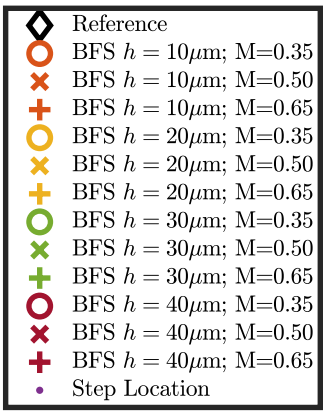

Fig. 5 Legend for Figs. 8, 9, 10, 11, 12, 53, 56, 57, 58 and 59

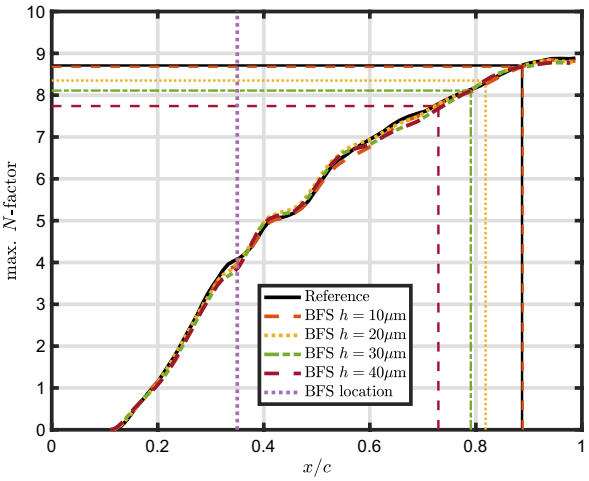

Fig. 6 Comparison of maximum N-factor distributions as a function of x/c for different step sizes. Transition N-factors are determined at the measured transition location for each configuration. The flow conditions are $\mathrm{Re}_1 = 22.5 \times 10^6\ \mathrm{m}^{-1}$, $M = 0.50$ and $H_{12} \approx 2.58$, which are the same as in Figs. 2 and 3. The purple dotted line marks the location of the step at $x_S/c = 0.35$

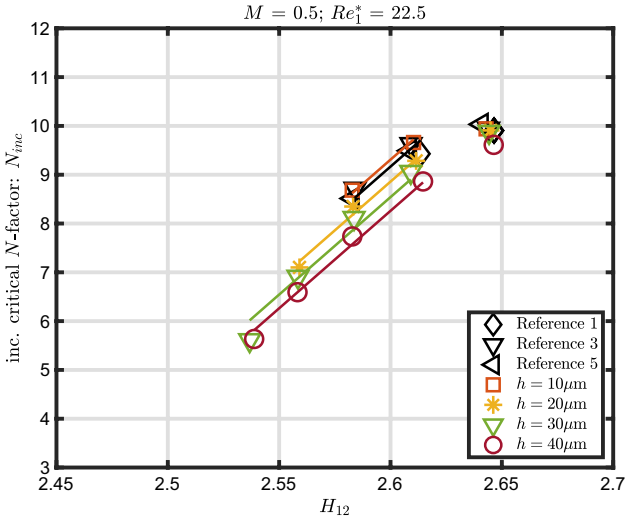

Fig. 7 Transition N-factors as a function of H_{12} for different reference configurations and step heights. The flow conditions are $M = 0.50$ and $\mathrm{Re}_1^* = 22.5$. The flow conditions are the same as in Fig. 4

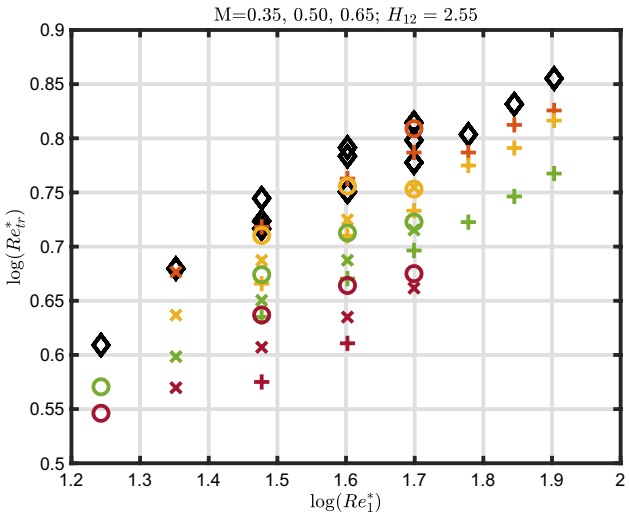

Fig. 8 Double logarithmic plot of Reynolds number Re_{tr} as a function of unit Reynolds number Re_1^* for all Mach numbers and model configurations at $H_{12} = 2.55$. The legend is shown in Fig. 5

values of Re_h (see Fig. 10). However, the considerations on this observation discussed with regard to the current data in Sect. 3.3 hold also for those reference data. In particular, a condition of $\xi = 1$ for $h/\delta_1 = 0$ and $\mathrm{Re}_h = 0$ may be deemed as a more suitable approximation of the data from Wang and Gaster (2005).

In any case, all data from the present and previous investigations show significant reduction of the laminar flow length at $\mathrm{Re}_h = 900$, which is the critical value for BFS reported in Nenni and Gluyas (1966); Schrauf (2018). In the present work, $\xi \approx 0.77$ was found at $\mathrm{Re}_h = 900$. For flow conditions analogous to those examined in the current and previous investigations (Perraud and Séraudie 2000; Wang and Gaster 2005; Hildebrand et al. 2020), this value of Re_h can therefore be maintained as 'critical' if a reduction in ξ by 0.2 is still acceptable for NLF design purposes; otherwise, even tighter tolerances may be necessary. The critical value of Re_h may be, however, higher for different boundary layer stability situations, such as in the case of an airfoil with a long region of accelerated flow followed by a strong adverse pressure gradient (e.g., for shock-induced transition).

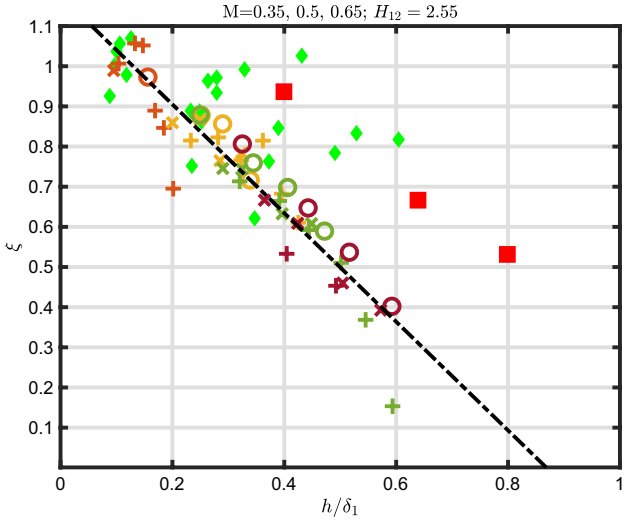

Fig. 9 The parameter ξ as a function of normalized step height h/δ_1 for all Mach numbers and configurations with $H_{12} = 2.55$. The two filled red squares resemble data points collected by Wang and Gaster (2005) at 34 m s^{-1} with step heights of 0.25 mm and 0.4 mm, and the filled green diamonds correspond to the measurement by Crouch et al. (2006), while the legend for all other data points is shown separately in Fig. 5

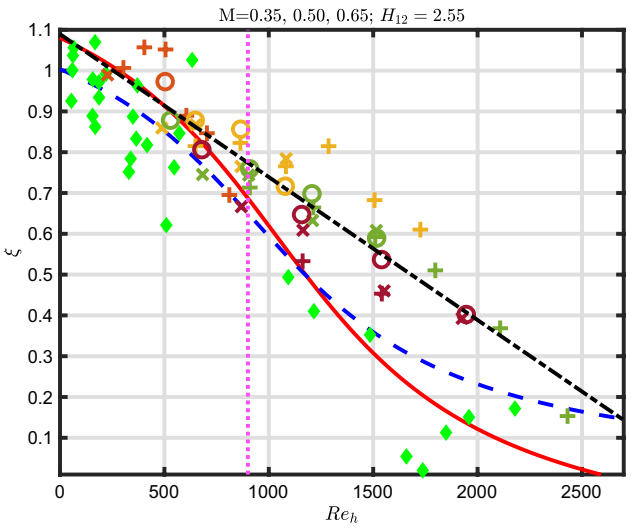

Fig. 10 The parameter ξ as a function of step-height Reynolds number Re_h for all Mach numbers and configurations with $H_{12} = 2.55$. The legend of the symbols is shown separately in Fig. 5. The red line corresponds to the measured transition data by Wang and Gaster (2005), the blue dashed line corresponds to the computational prediction by Hildebrand et al. (2020), the vertical magenta dotted line corresponds to the criterion from Nenni and Gluyas (1966), and the filled green diamonds correspond to the measurement by Crouch et al. (2006), while the black dash-dotted line corresponds to a linear fit of the data in the current study

Table 2 Slopes (m) and intercepts (b) of ξ as a function of h/δ_1 and ξ as a function of Re_h for different shape factors H_{12}

H_{12}	h/δ_1 Slope	h/δ_1 Intercept	Re_h Slope	Re_h Intercept
2.30	−1.366	1.187	−3.16d-4	1.060
2.40	−1.368	1.189	−3.20d-4	1.064
2.50	−1.366	1.189	−3.29d-4	1.075
2.55	−1.353	1.176	−3.50d-4	1.089

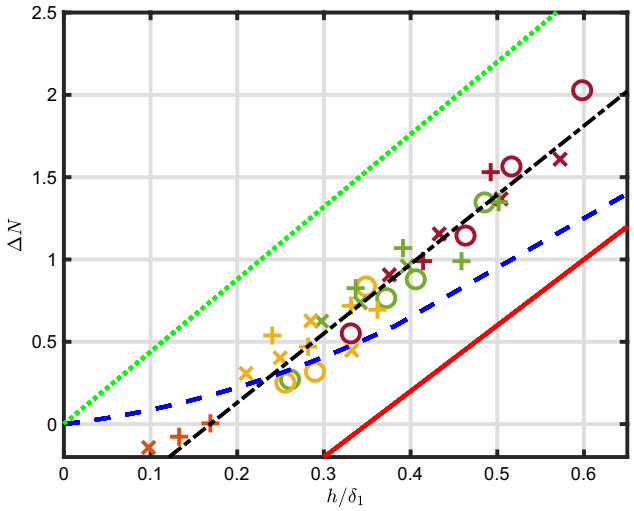

Fig. 11 Impact of the BFS on the transition N-factor, ΔN, plotted against normalized step height, h/δ_1. The legend of the symbols is shown separately in Fig. 5. The red line corresponds to the data by Wang and Gaster (2005), the blue dashed line corresponds to the computational prediction by Hildebrand et al. (2020), the green dotted line corresponds to the data by Crouch et al. (2006); Crouch and Kosorygin (2020), and the black dash-dotted line corresponds to a linear fit of the data in the current study

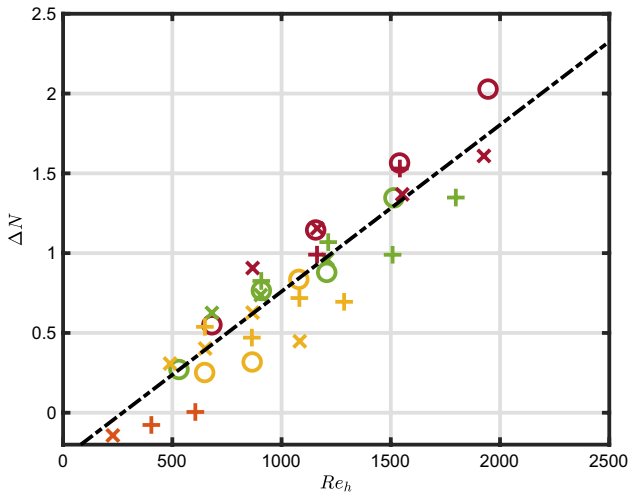

Fig. 12 Impact of the BFS on the transition N-factor, ΔN, plotted as a function of step-height Reynolds number, Re_h. The legend is shown separately in Fig. 5

3.5 Influence of the step height on the *N*-factor

In parallel to the study on the influence of gaps (Risius et al. 2023) also in the current investigation, the transition *N*-factor was assumed to be linearly dependent on H_{12}, which was found to be a good approximation for $H_{12} \lesssim 2.59$ (see Sect. 2.5). Based on this approximation, it is possible to calculate the offset in the transition *N*-factors by different configurations: $\Delta N = N_{\text{reference}} - N_{\text{BFS}}$. In the decelerated region with $H_{12} \gtrsim 2.59$, the influence of BFS on the *N*-factor cannot be quantified in terms of ΔN as the transition *N*-factor reaches a common plateau region (see, for example, Figs. 19 and 25).

The change of the transition *N*-factor, ΔN, is shown as a function of the relative step height h/δ_1 in Fig. 11. It shows that an increasing step height leads to an increasing ΔN. The average approximation is $\Delta N \approx 4.2 \cdot h/\delta_1 - 0.71$ (black dashed line), which may be used as a rule of thumb to estimate the expected reduction of the transition *N*-factor for approximately $h/\delta_1 > 0.17$: In practice, a BFS with 40% height of the displacement thickness at the BFS location would lead to a reduction of the transition *N*-factor of $\Delta N \approx 1 \pm 0.25$.

In agreement with the results on the influence of gaps (Risius et al. 2023), the transition *N*-factor is reduced and ΔN increases almost linearly with relative imperfection size (h/δ_1 here, see Fig. 11). These findings are also in agreement with the general trends reported by Wang and Gaster (2005); Crouch et al. (2006); Crouch and Kosorygin (2020); Hildebrand et al. (2020) as shown in Fig. 11. The results from Wang and Gaster (2005), however, predict a smaller influence of the BFS on N_{tr}, and the results from Crouch et al. (2006) and Crouch and Kosorygin (2020) predict a larger influence of the BFS. The current results are closer to the predictions by Hildebrand et al. (2020). The ΔN functions from Wang and Gaster (2005) and Crouch et al. (2006); Crouch and Kosorygin (2020) may therefore be used as best- and worst-case scenarios, respectively, for the prediction of the impact of BFS on transition. The considerations on the negative values of ΔN and on the possible reasons for the differences in ΔN-values are analogous to those discussed above for ξ and are therefore not repeated here. Nevertheless, it should be emphasized that the slope of the present linear approximation curve ($\Delta N/(h/\delta_1) = 4.2$) and that from Crouch et al. (2006); Crouch and Kosorygin (2020) ($\Delta N/(h/\delta_1) = 4.4$) are in excellent agreement, indicating a comparable effect of the BFS on the transition *N* factors once an upstream transition shift sets in.

An analysis similar to that of Fig. 11 can be performed with ΔN as a function of the step-height Reynolds number, Re_h, as shown in Fig. 12. The general trend of an increasing ΔN with step height of the BFS, with an almost linear dependency, can also be seen in this case. The expected increase of ΔN is given by

$$\Delta N = 1.044 \times 10^{-3} \cdot \text{Re}_h - 0.2844 \text{ (black dashed line)},$$

which may also be used as a rule of thumb to estimate the expected reduction of the transition *N*-factor at approximately $\text{Re}_h > 270$: In practice, a reduction of a transition *N*-factor by $\Delta N \approx 1 \pm 0.25$ is reached at $\text{Re}_h \approx 1230$.

In summary, the current results about the dependency of ΔN on step height are found to be in agreement with the literature and extend the available data to various pressure gradients and significantly larger Mach and Reynolds number ranges. However, they focus on favorable pressure gradients. The influence of BFS on ΔN was investigated for two different pressure gradients in Crouch and Kosorygin (2020), being obtained by placing the steps in two different regions of the examined, non-uniform pressure distribution. For the adverse pressure gradient region, the linear function $\Delta N = 4.4 \cdot h/\delta_1$ provided a reasonable approximation of the relation between ΔN and h/δ_1, while it represented a rough upper bound to the data obtained in the favorable pressure gradient region (with steps placed at a location upstream of the point of indifferent stability of T-S waves). Thus, it may be inferred that smaller values of ΔN were obtained for favorable pressure gradient; however, the data presented appreciable scatter, and the above reported considerations (step upstream of indifferent stability point, non-uniform pressure gradient in the investigated region $x_{T0} - x_S$) should be also taken into account. The present considerations for the examined adverse pressure gradients (see Sect. 2.5) and the observations reported in Crouch and Kosorygin (2020) suggest to conduct a dedicated investigation to evaluate in more detail the applicability of the ΔN model for decelerated boundary layers at the conditions considered in the present work.

4 Conclusions

In conclusion, we may emphasize that this study shows a systematic investigation of the effects of backward-facing steps on transition Reynolds numbers and transition *N*-factors at various pressure gradients, Mach and Reynolds numbers. The influence of four different BFS sizes is investigated at subsonic flow speeds at high Reynolds numbers. The measured temperature and pressure distributions are used as input for boundary layer calculations and linear stability analysis. By correlation with the measured transition locations, transition *N*-factors are determined, and the influence of BFS is quantified by the ΔN-method. The transition Reynolds numbers and transition *N*-factors of six wind tunnel

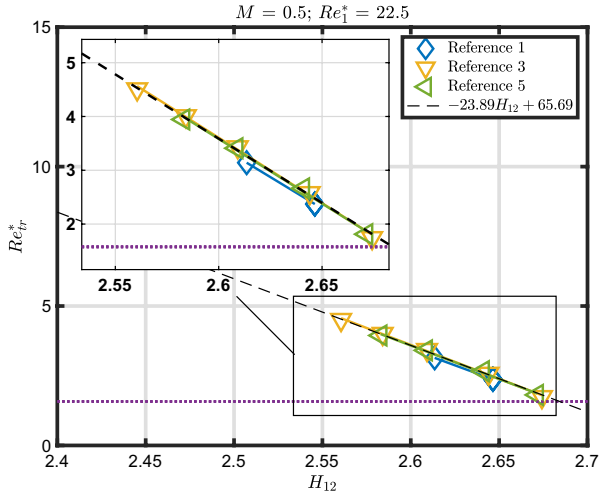

Fig. 13 Approximation of the influence of H_{12} on the transition Reynolds number for the reference configuration, which was measured in three different wind tunnel entries (labeled as 'Reference 1,' 'Reference 3' and 'Reference 5,' where the number specifies the number of the wind tunnel entry). The fitted averaged function is shown as dashed black line. For better comparability, the scale of H_{12} and Re_{tr} in the main figure was chosen to be identical with the scale in the figures in Appendix (Figs. 14, 17, 20, 23, 26, 29, 32, 35, 38, 41, 44, 47, 50). A zoomed area is shown in this figure as an inset

entries of the reference configuration over two years show a very good repeatability of the test results.

The installation of BFS with 10 µm height does not lead to a reduction of Re_{tr} and transition N-factors within the measurement accuracy. Increasing the step size to $h = 20\,\mu\mathrm{m}$, $h = 30\,\mu\mathrm{m}$ or $h = 40\,\mu\mathrm{m}$ results in an increasing reduction of the transition Reynolds number and transition N-factor.

The relative change in transition location with respect to the step location ($\xi = (x_T - x_S)/(x_{T0} - x_S)$) and the step-induced ΔN is investigated as a function of the non-dimensional step parameters h/δ_1 and Re_h. For steps with $h/\delta_1 > 0.17$ and $\mathrm{Re}_h > 270$, the present results are well approximated by linear functions. The observed trends for ξ are qualitatively in agreement with earlier measurements in other wind tunnels at lower Mach and unit Reynolds numbers for small values of h/δ_1, whereas quantitative agreement was found up to $\mathrm{Re}_h \approx 800$. The critical value of $\mathrm{Re}_h = 900$ reported in the literature was shown to correspond to $\xi \approx 0.8$ in the present results.

The influence of the BFS on the transition N-factor was found to be $\Delta N = 4.2 \cdot h/\delta_1 - 0.71$, which can be used to estimate the effect of the BFS on transition for the examined flow conditions at approximately $h/\delta_1 > 0.17$. The variation of ΔN in this case is similar to the results from Hildebrand et al. (2020) and shows an intermediate impact of BFS as compared to those reported in Wang and Gaster (2005) and Crouch et al. (2006); Crouch and Kosorygin (2020).

By this systematic investigation, it was found that the Mach number has no significant influence on the transition Reynolds number Re_{tr} under the described experimental conditions with installed BFS, which is in agreement with the results with gaps (Risius et al. 2023). It was found that Re_{tr} increases with Re_1, which is known as 'unit Reynolds number effect.' The slope α_{III} of the relation $\mathrm{Re}_{tr}^* \sim \left(\mathrm{Re}_1^*\right)^{\alpha_{III}}$ was found to vary between 0.4 and 0.7, in agreement with earlier investigations (Risius et al. 2018b, 2023). The measurement at different pressure gradients allowed to compare the BFS influence at different H_{12}. In agreement with similar investigations on the influence of gaps (Risius et al. 2023) and forward-facing steps (Costantini 2016; Costantini et al. 2022), the results show that the relative influence of backward-facing steps causes a stronger reduction of Re_{tr} at smaller H_{12}, corresponding to stronger favorable pressure gradients. Nevertheless, the evaluation of the results with ξ as a function of h/δ_1 and Re_h enabled to isolate the effect of the BFS on boundary layer transition, since the relations between these parameters are shown to be essentially unaffected by variations in Mach number, unit Reynolds number and pressure gradient. This result is in line with previous findings for FFS (Costantini 2016; Costantini et al. 2022). It should be remarked here that the present results are valid for examined range of parameters and boundary layer stability situations, beyond which further investigations would be necessary to verify the validity of the obtained correlations.

In summary, the described results, achieved at subsonic Mach numbers and flight-relevant Reynolds numbers for different streamwise pressure gradient, provide valuable support for the design of laminar surfaces with transition scenarios dominated by Tollmien–Schlichting instabilities. The correlations of the experimental data can be used to define appropriate maximum steps sizes and manufacturing tolerances as well as to validate numerical predictions, whereas the ΔN-functions can be considered in the design process for an estimation of the impact of BFS on transition.

Appendix

Details of data acquisition and analysis

The *PaLASTra* model was repeatedly tested in KRG with four different step sizes in six separate measurement campaigns over a time span of two years. The reference configuration (without an installed step) was re-tested in each measurement campaign. A good repeatability of the measured transition locations was observed, as shown exemplarily in Fig. 13 (for the first, third and fifth measurement campaign) and systematically in Appendix (Figs. 14, 17, 20, 23, 26, 29, 32, 35, 38, 41).

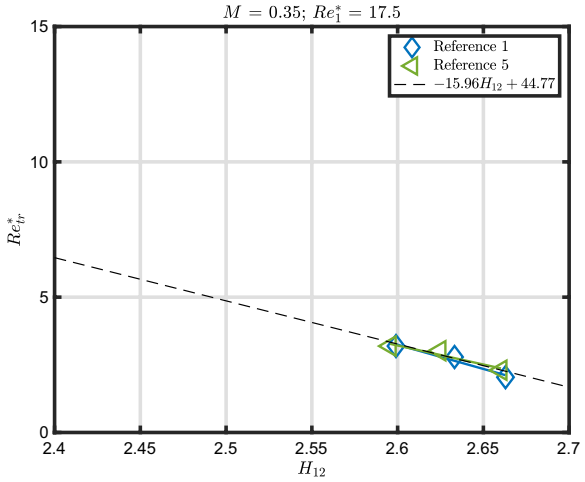

Fig. 14 $\mathrm{Re}_{\mathrm{tr}}^*$ as a function of H_{12} for the reference configuration

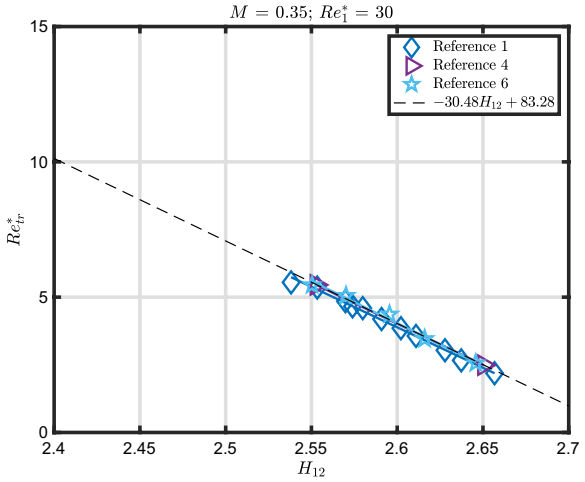

Fig. 17 $\mathrm{Re}_{\mathrm{tr}}^*$ as a function of H_{12} for the reference configuration

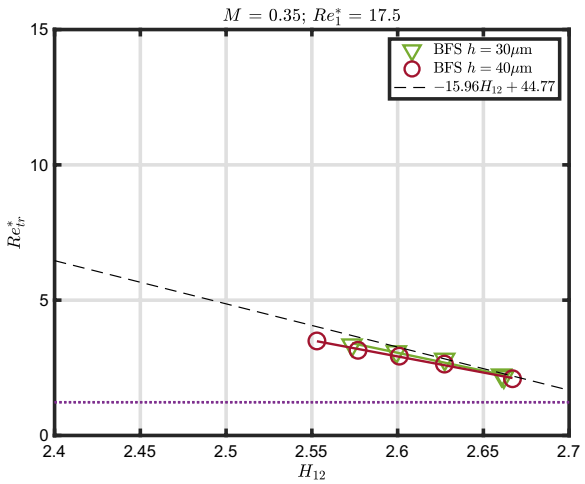

Fig. 15 $\mathrm{Re}_{\mathrm{tr}}^*$ as a function of H_{12} for the configurations with steps

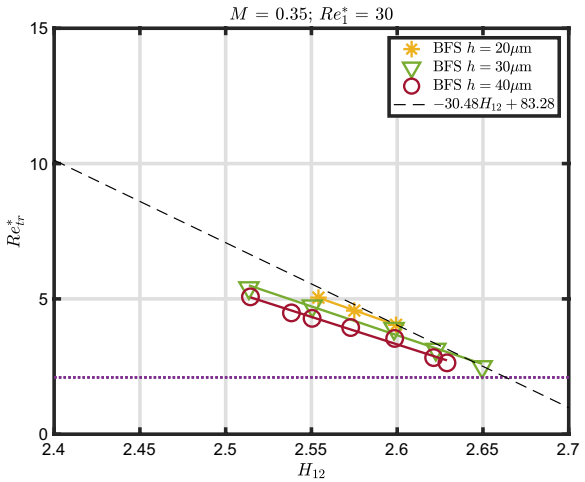

Fig. 18 $\mathrm{Re}_{\mathrm{tr}}^*$ as a function of H_{12} for the configurations with steps

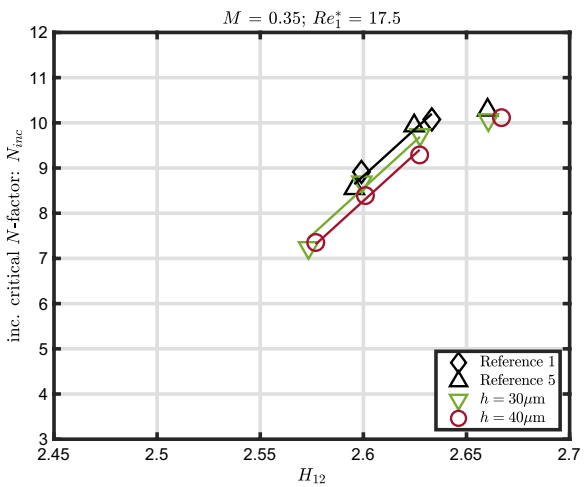

Fig. 16 Inc. transition N-factors as a function of H_{12} for different reference configurations and step heights with $M = 0.35$, $\mathrm{Re}_1^* = 17.5$

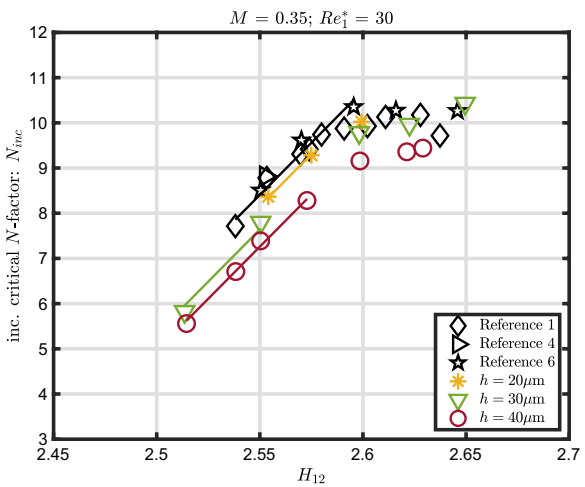

Fig. 19 Inc. transition N-factors as a function of H_{12} for different reference configurations and step heights with $M = 0.35$, $\mathrm{Re}_1^* = 30$

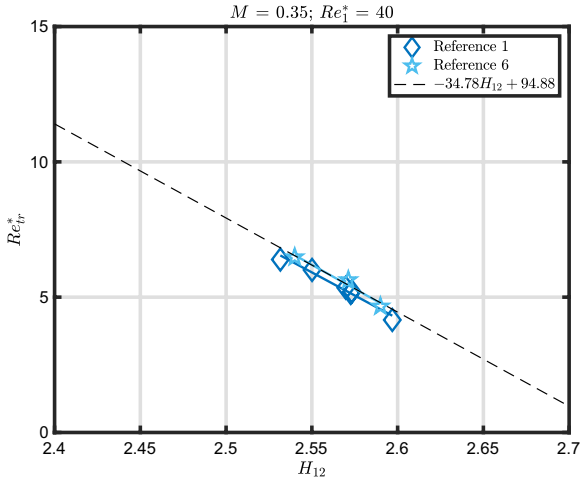

Fig. 20 $\mathrm{Re}_{\mathrm{tr}}^*$ as a function of H_{12} for the reference configuration

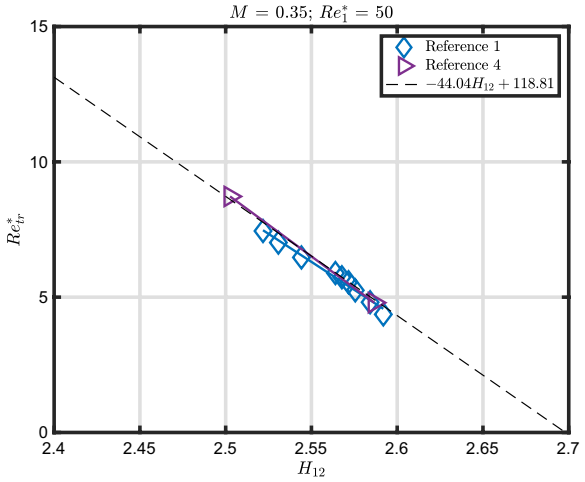

Fig. 23 $\mathrm{Re}_{\mathrm{tr}}^*$ as a function of H_{12} for the reference configuration

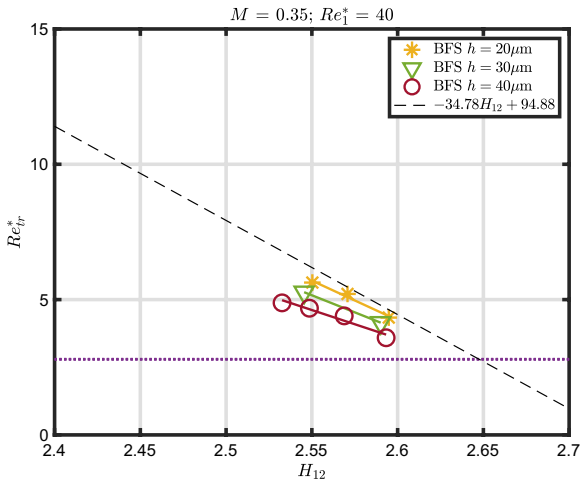

Fig. 21 $\mathrm{Re}_{\mathrm{tr}}^*$ as a function of H_{12} for the configurations with steps

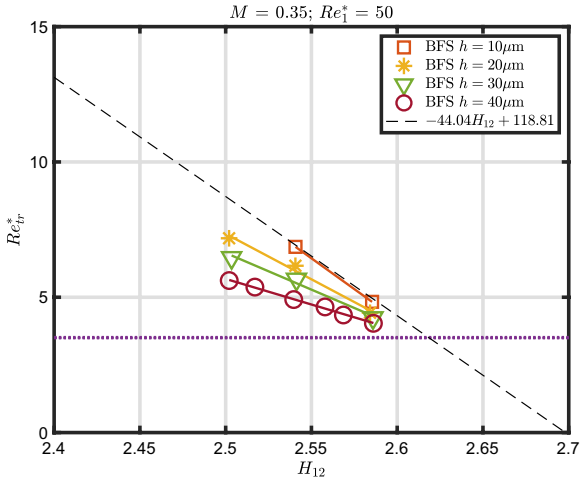

Fig. 24 $\mathrm{Re}_{\mathrm{tr}}^*$ as a function of H_{12} for the configurations with steps

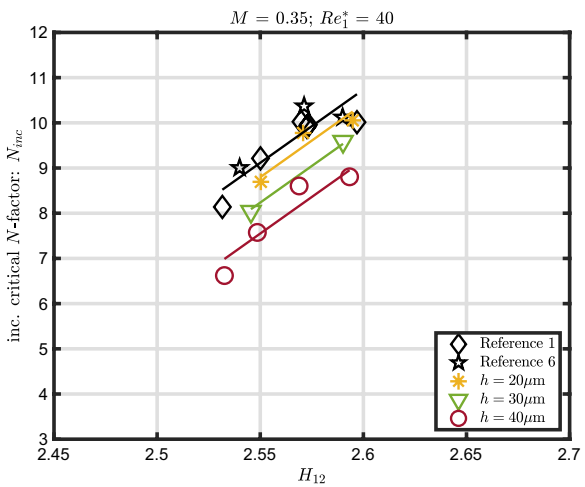

Fig. 22 Inc. transition N-factors as a function of H_{12} for different reference configurations and step heights with $M = 0.35$, $\mathrm{Re}_1^* = 40$

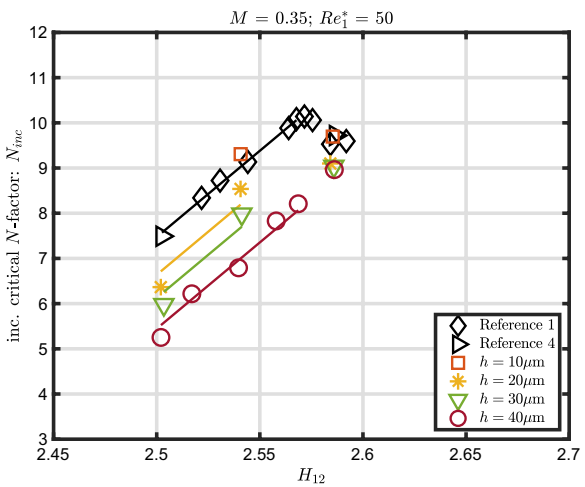

Fig. 25 Inc. transition N-factors as a function of H_{12} for different reference configurations and step heights with $M = 0.35$, $\mathrm{Re}_1^* = 50$

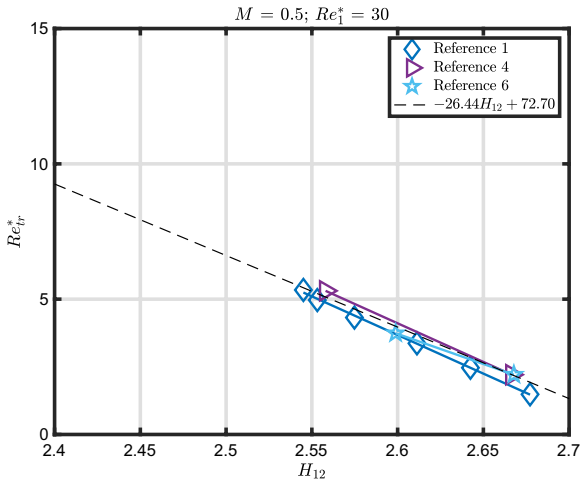

Fig. 26 $\mathrm{Re}_{\mathrm{tr}}^*$ as a function of H_{12} for the reference configuration

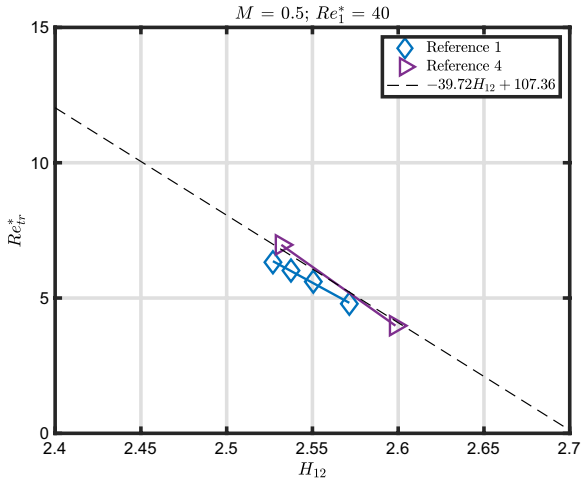

Fig. 29 $\mathrm{Re}_{\mathrm{tr}}^*$ as a function of H_{12} for the reference configuration

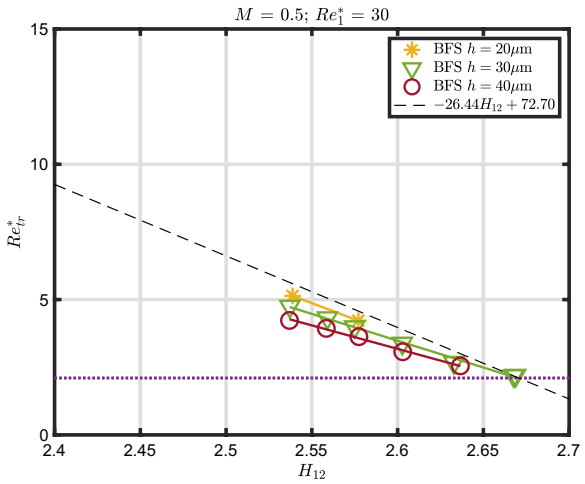

Fig. 27 $\mathrm{Re}_{\mathrm{tr}}^*$ as a function of H_{12} for the configurations with steps

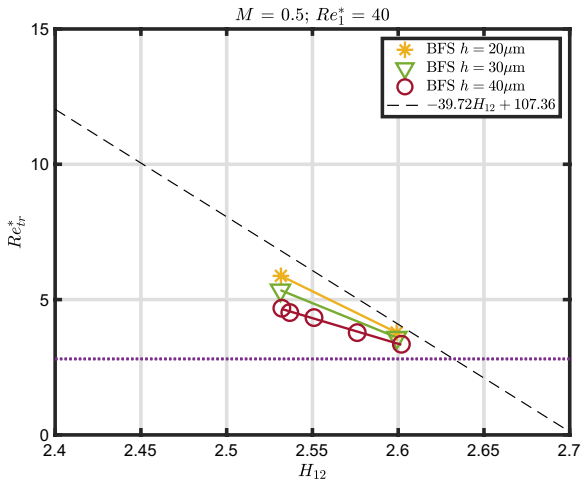

Fig. 30 $\mathrm{Re}_{\mathrm{tr}}^*$ as a function of H_{12} for the configurations with steps

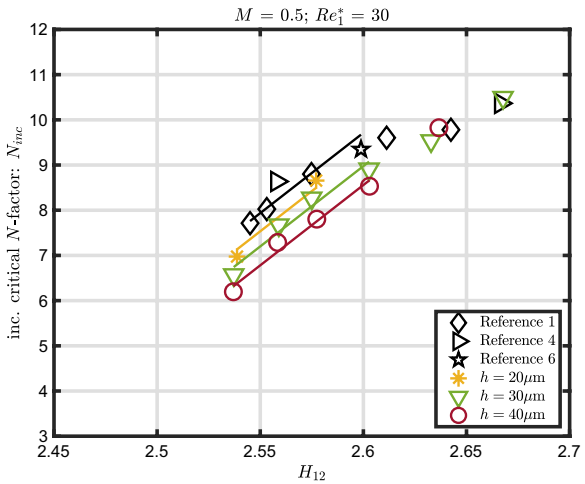

Fig. 28 Inc. transition N-factors as a function of H_{12} for different reference configurations and step heights with $M = 0.50$, $\mathrm{Re}_1^* = 30$

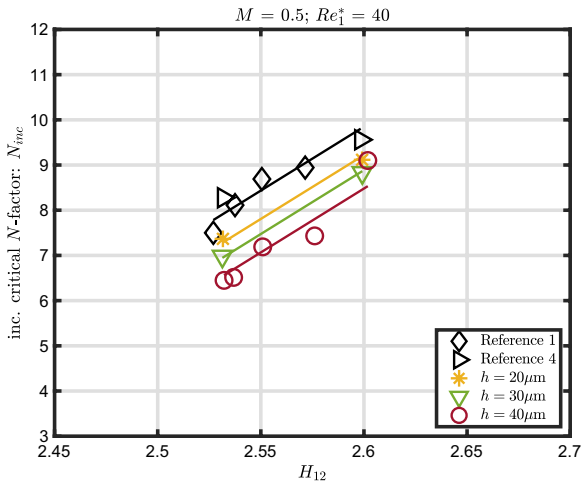

Fig. 31 Inc. transition N-factors as a function of H_{12} for different reference configurations and step heights with $M = 0.50$, $\mathrm{Re}_1^* = 40$

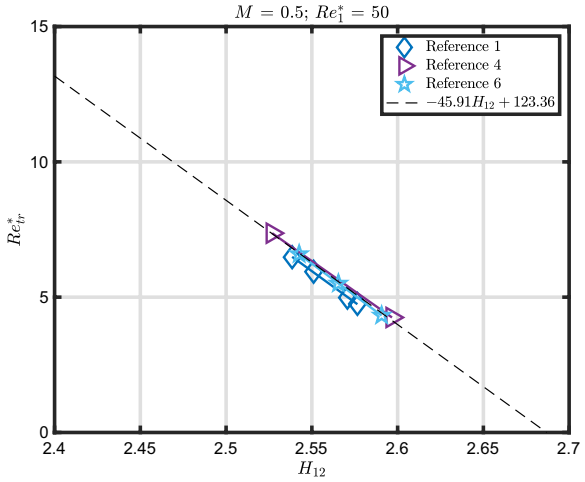

Fig. 32 $\mathrm{Re}_{\mathrm{tr}}^*$ as a function of H_{12} for the reference configuration

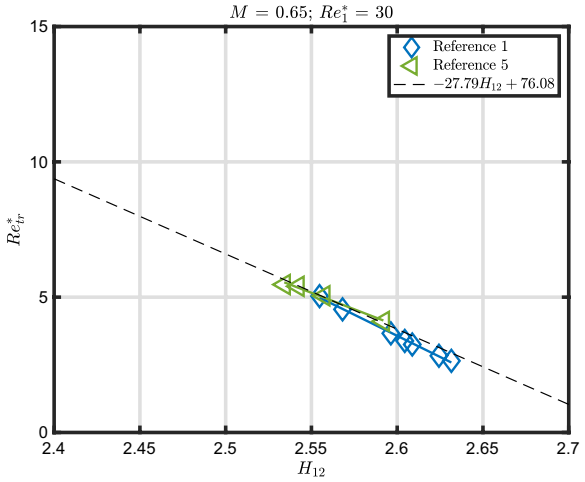

Fig. 35 $\mathrm{Re}_{\mathrm{tr}}^*$ as a function of H_{12} for the reference configuration

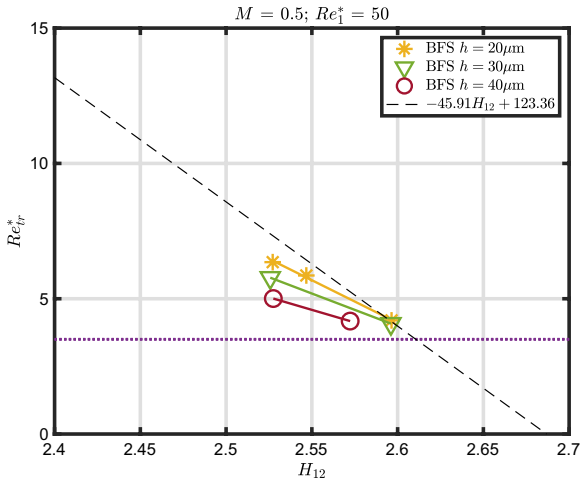

Fig. 33 $\mathrm{Re}_{\mathrm{tr}}^*$ as a function of H_{12} for the configurations with steps

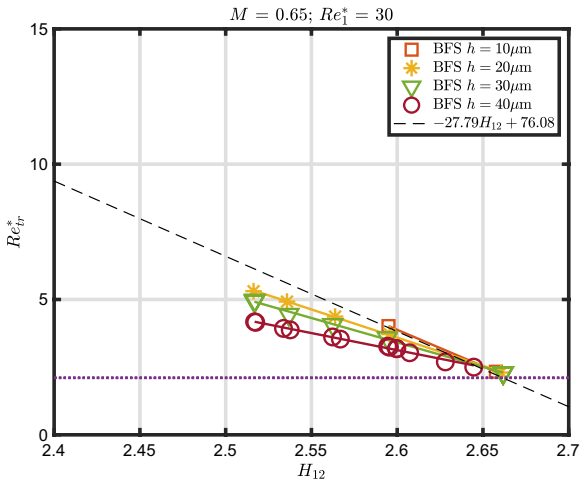

Fig. 36 $\mathrm{Re}_{\mathrm{tr}}^*$ as a function of H_{12} for the configurations with steps

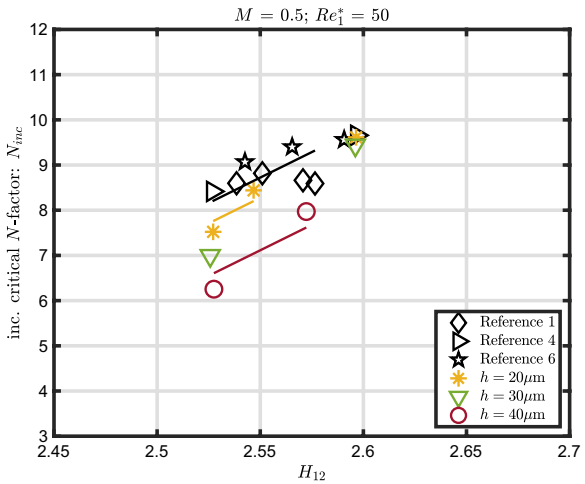

Fig. 34 Inc. transition N-factors as a function of H_{12} for different reference configurations and step heights with $M = 0.50$, $\mathrm{Re}_1^* = 50$

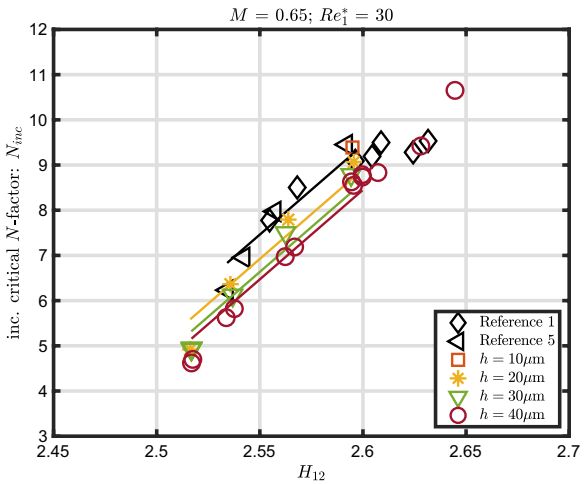

Fig. 37 Inc. transition N-factors as a function of H_{12} for different reference configurations and step heights with $M = 0.65$, $\mathrm{Re}_1^* = 30$

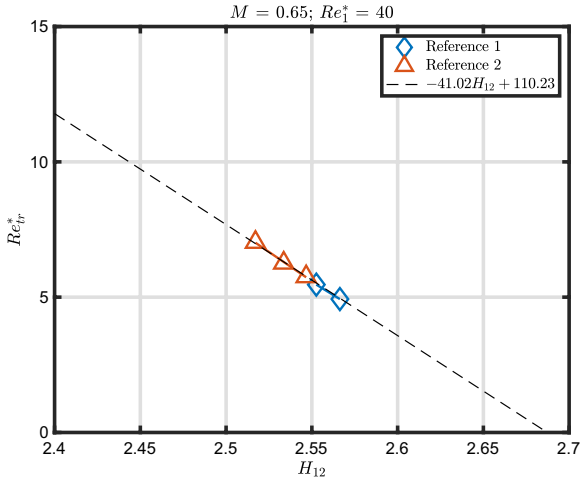

Fig. 38 $\mathrm{Re}_{\mathrm{tr}}^*$ as a function of H_{12} for the reference configuration

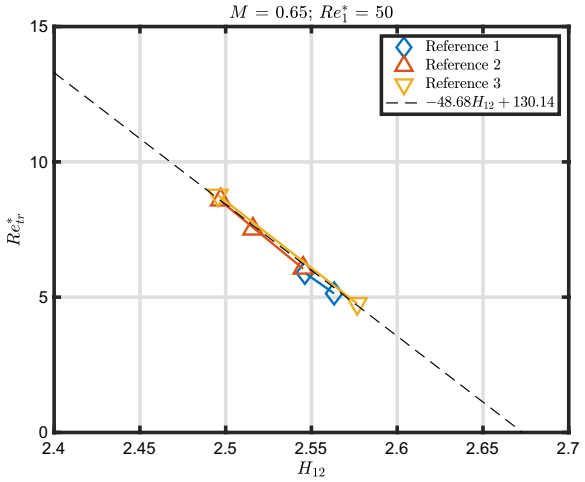

Fig. 41 $\mathrm{Re}_{\mathrm{tr}}^*$ as a function of H_{12} for the reference configuration

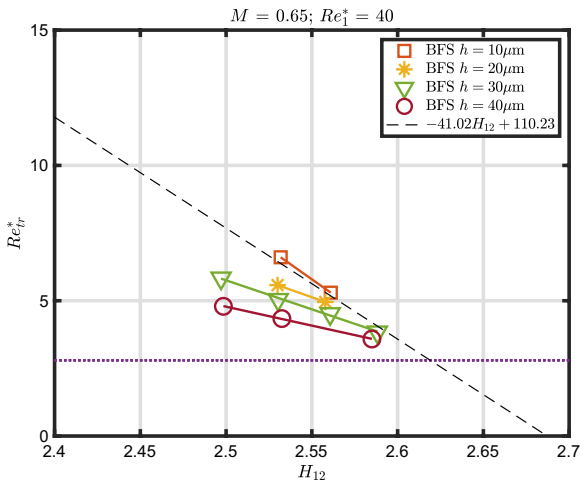

Fig. 39 $\mathrm{Re}_{\mathrm{tr}}^*$ as a function of H_{12} for the configurations with steps

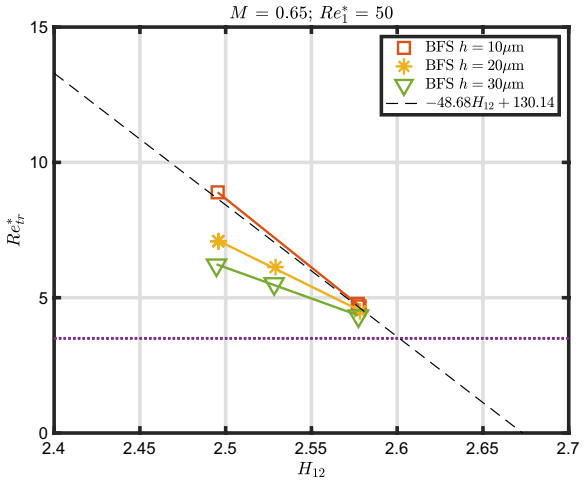

Fig. 42 $\mathrm{Re}_{\mathrm{tr}}^*$ as a function of H_{12} for the configurations with steps

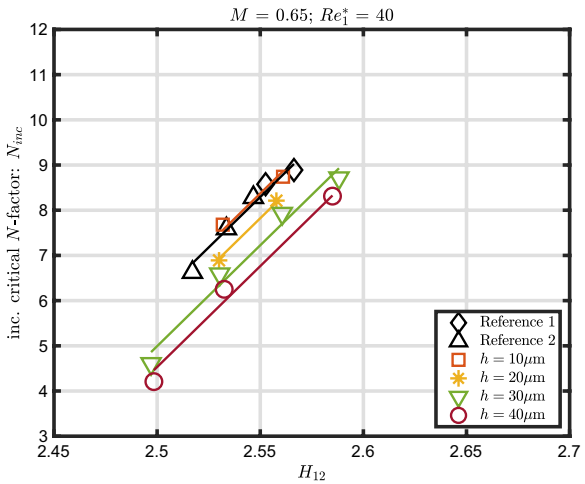

Fig. 40 Inc. transition N-factors as a function of H_{12} for different reference configurations and step heights with $M = 0.65$, $\mathrm{Re}_1^* = 40$

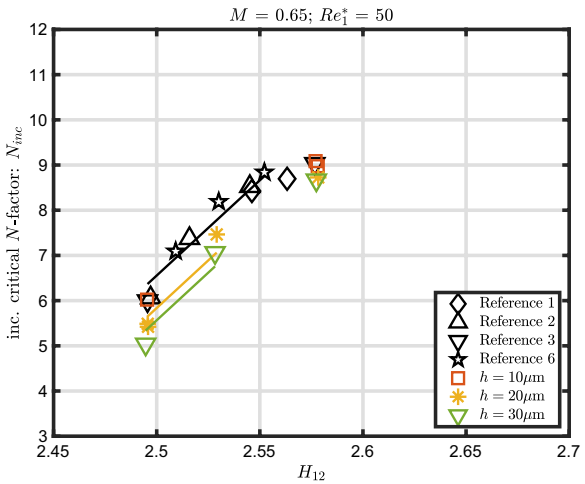

Fig. 43 Inc. transition N-factors as a function of H_{12} for different reference configurations and step heights with $M = 0.65$, $\mathrm{Re}_1^* = 50$

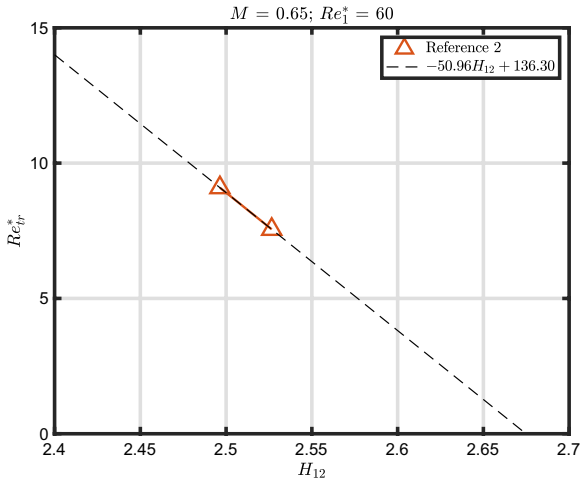

Fig. 44 $\mathrm{Re}_{\mathrm{tr}}^*$ as a function of H_{12} for the reference configuration

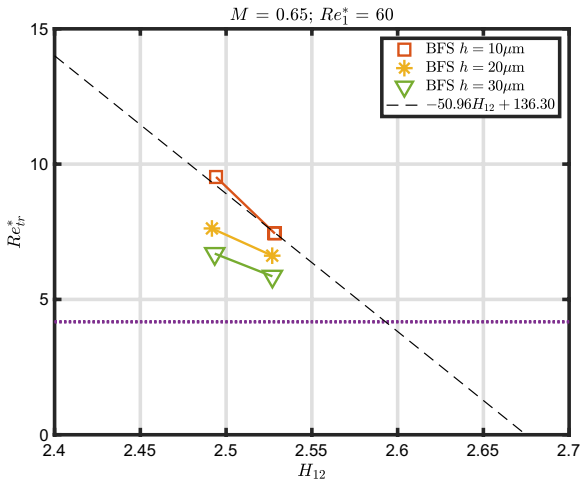

Fig. 45 $\mathrm{Re}_{\mathrm{tr}}^*$ as a function of H_{12} for the configurations with steps

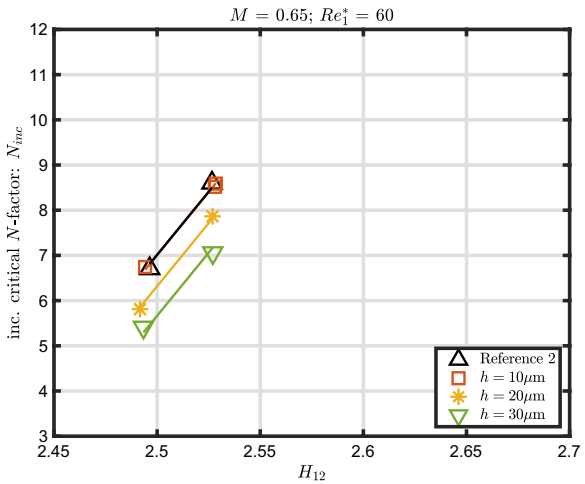

Fig. 46 Inc. transition N-factors as a function of H_{12} for different reference configurations and step heights with $M = 0.65$, $\mathrm{Re}_1^* = 60$

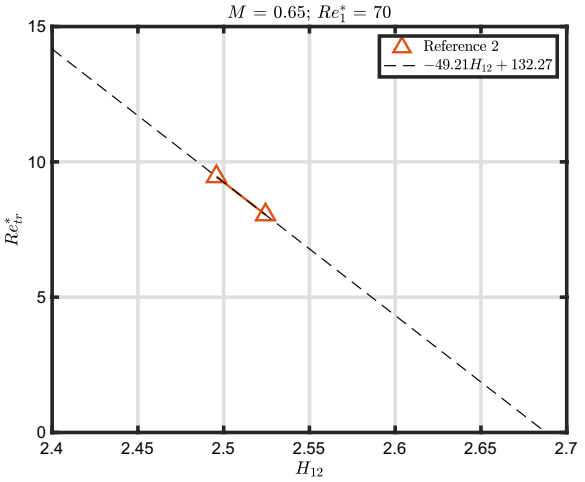

Fig. 47 $\mathrm{Re}_{\mathrm{tr}}^*$ as a function of H_{12} for the reference configuration

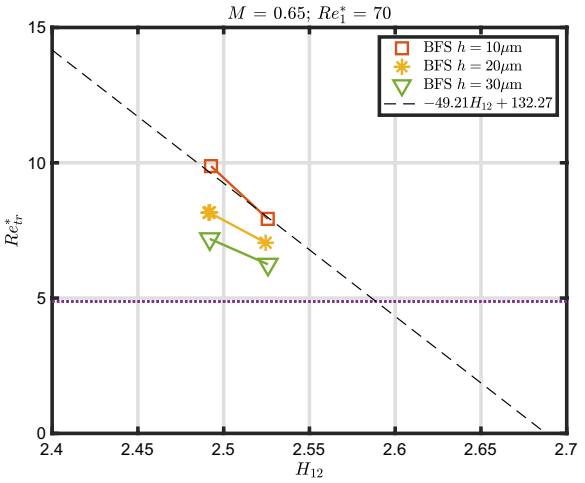

Fig. 48 $\mathrm{Re}_{\mathrm{tr}}^*$ as a function of H_{12} for the configurations with steps

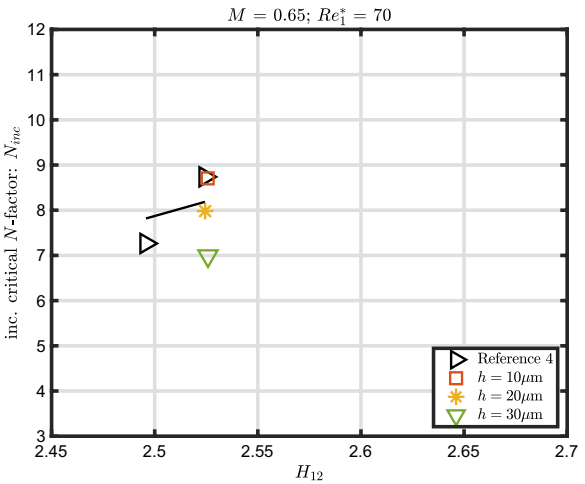

Fig. 49 Inc. transition N-factors as a function of H_{12} for different reference configurations and step heights with $M = 0.65$, $\mathrm{Re}_1^* = 70$

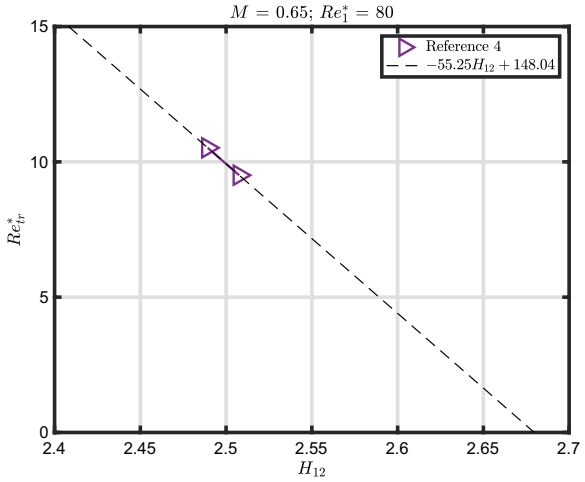

Fig. 50 $\mathrm{Re}_{\mathrm{tr}}^*$ as a function of H_{12} for the reference configuration

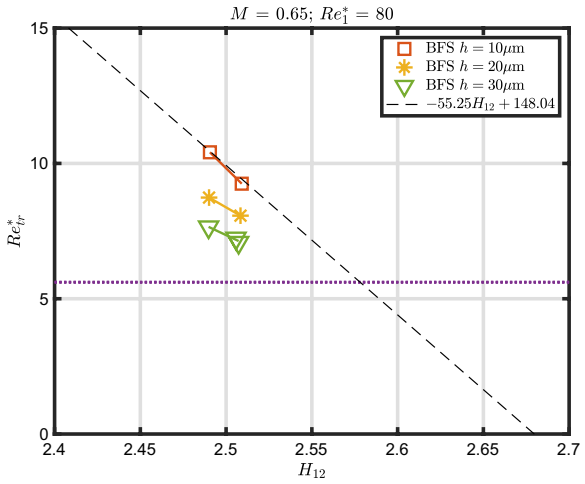

Fig. 51 $\mathrm{Re}_{\mathrm{tr}}^*$ as a function of H_{12} for the configurations with steps

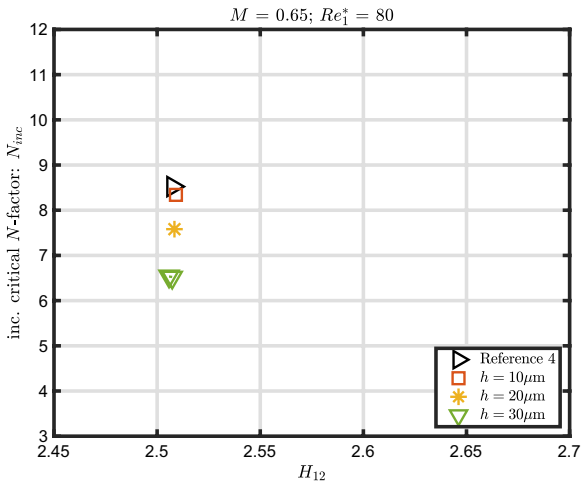

Fig. 52 Inc. transition N-factors as a function of H_{12} for different reference configurations and step heights with $M = 0.65$, $\mathrm{Re}_1^* = 80$

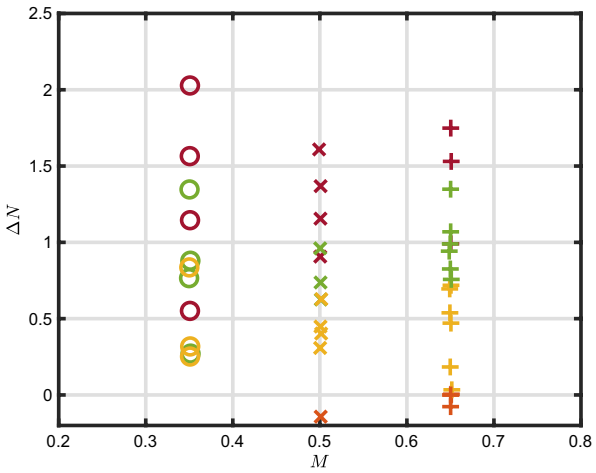

Fig. 53 Relative reduction of the transition N-factor, ΔN, caused by the step, plotted as a function of Mach number M. The legend is shown separately in Fig. 5

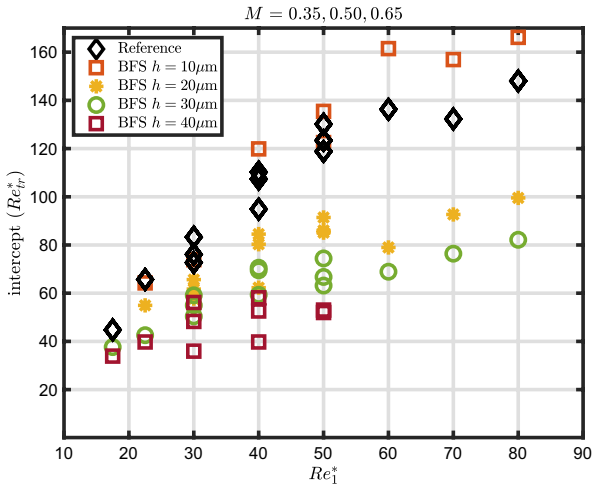

Fig. 54 Intercepts, $h_{II,0}$, of the linear approximation for all data points

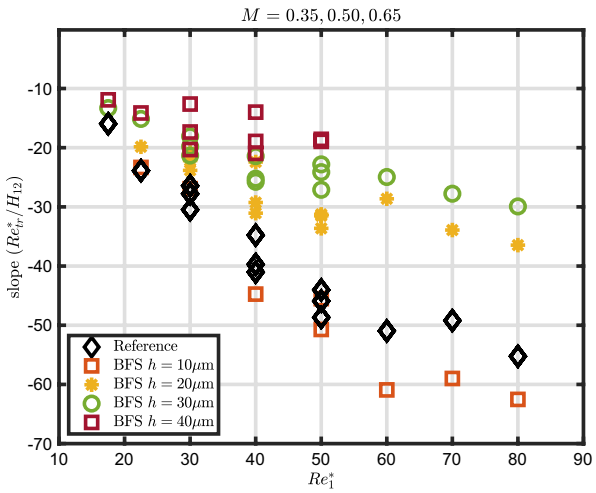

Fig. 55 Slopes, $h_{II,1}$, of the linear approximation for all data points

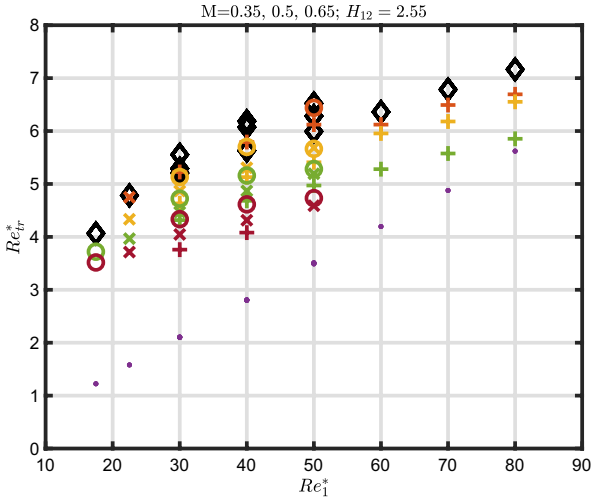

Fig. 56 Calculated transition Reynolds number Re_{tr} as a function of unit Reynolds number Re^*_1 for all Mach numbers and $H_{12} = 2.55$. The purple dots mark the Reynolds number corresponding to the location of the step. The legend is shown separately in Fig. 5

The transition detection was carried out with TSP over almost the complete span at up to 300 separate spanwise sections by the maximal gradient technique (Costantini et al. 2021). For each section, the maximum intensity gradient in flow direction was determined and marked by a red dot which highlights the determined transition location. Each TSP image in Fig. 3 shows a laminar region on the left (light gray) and a turbulent region on the right (dark). A turbulent wedge in the mid-span domain is caused by pressure taps in the spanwise center of the model, which was excluded from transition detection.

Side wall effects (visible at top and bottom of Fig. 3) and turbulent wedges (in the middle of Fig. 3) caused by surface contamination or pressure taps were excluded from the transition detection (Risius et al. 2018b; Costantini et al. 2021). The RMS of the variation in transition location along the span was determined for each data point and used to quantify the measurement uncertainty of the transition location, which was typically within $\Delta x/c = 1\%$.

In order to determine the surface temperature distribution on the upper side of the model, the TSP was calibrated in an external calibration chamber (Egami et al. 2012) and thermocouples integrated into the TSP layer were used to measure reference temperatures (Risius et al. 2018b). Surface temperature distributions in the streamwise direction, which were extracted from the TSP data at five spanwise sections, were averaged to obtain the streamwise surface temperature profile. The measured surface temperature and pressure distributions were then used as inputs for boundary layer calculations, as described in Risius et al. (2018b) and summarized in Sect. 2.4.

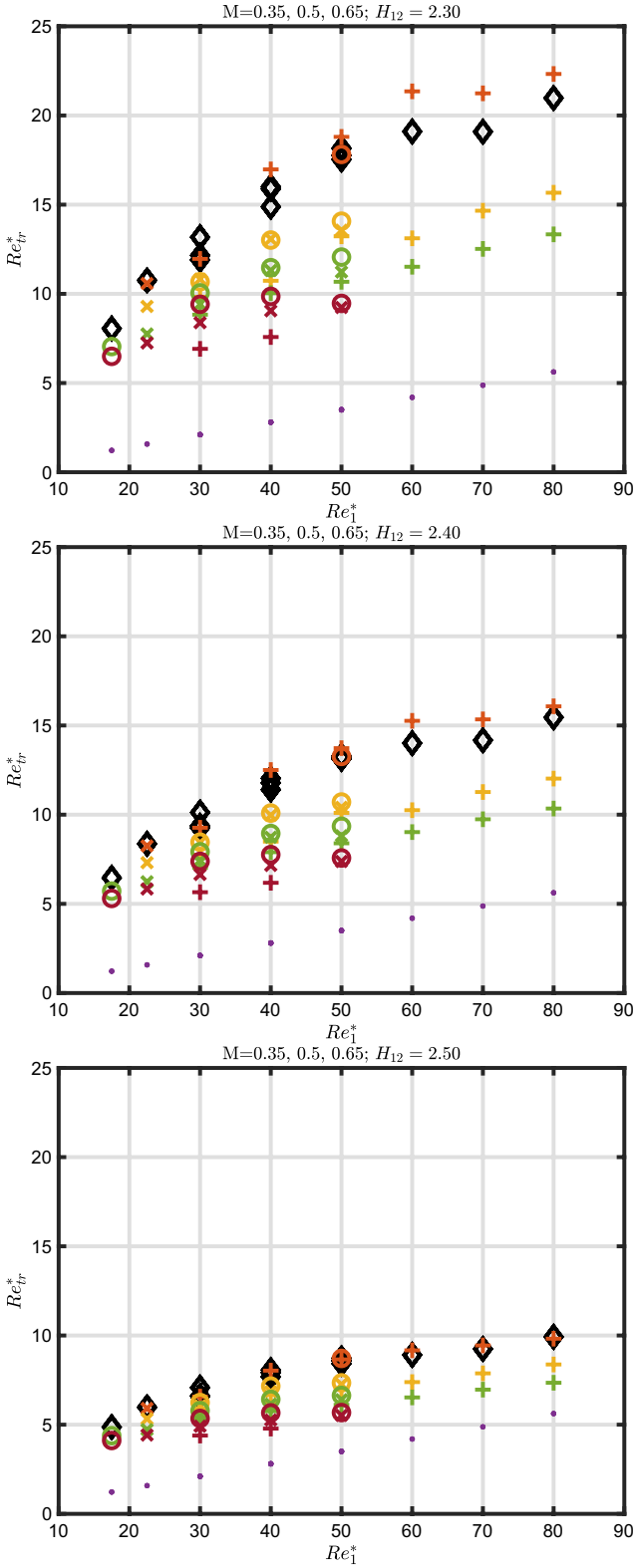

Fig. 57 Calculated transition Reynolds number Re_{tr} as a function of unit Reynolds number Re^*_1 for all Mach numbers and $H_{12} = 2.30$, 2.40 and 2.50 . The purple dots mark the Reynolds number corresponding to the location of the step. The legend is shown separately in Fig. 5

Table 3 Intercepts, $h_{II,0}$, of configuration with $h = 10\,\mu m$ as a function of unit Reynolds number and Mach number (see Eq. 2)

Re_1^*	$M = 0.35$	$M = 0.50$	$M = 0.65$
17.5			
22.5		64.26	
30.0			73.90
40.0			119.88
50.0	122.48		135.44
60.0			161.48
70.0			156.93
80.0			166.14

Table 4 Intercepts, $h_{II,0}$, of configuration with $h = 20\,\mu m$ as a function of unit Reynolds number and Mach number (see Eq. 2)

Re_1^*	$M = 0.35$	$M = 0.50$	$M = 0.65$
17.5			
22.5		54.95	
30.0	61.69	65.64	57.72
40.0	80.31	84.51	62.29
50.0	91.42	86.04	85.13
60.0			78.98
70.0			92.67
80.0			99.53

Table 5 Intercepts, $h_{II,0}$, of configuration with $h = 30\,\mu m$ as a function of unit Reynolds number and Mach number (see Eq. 2)

Re_1^*	$M = 0.35$	$M = 0.50$	$M = 0.65$
17.5	37.64		
22.5		42.57	
30.0	59.11	54.96	50.39
40.0	69.49	70.56	59.33
50.0	74.42	66.74	63.16
60.0			68.91
70.0			76.40
80.0			82.16

Table 6 Intercepts, $h_{II,0}$, of configuration with $h = 40\,\mu m$ as a function of unit Reynolds number and Mach number (see Eq. 2)

Re_1^*	$M = 0.35$	$M = 0.50$	$M = 0.65$
17.5	33.90		
22.5		39.76	
30.0	56.15	48.29	35.96
40.0	58.08	52.61	39.76
50.0	53.00	51.99	
60.0			
70.0			
80.0			

Table 7 Slopes, $h_{II,1}$, of configuration with $h = 10\,\mu m$ as a function of unit Reynolds number and Mach number (see Eq. 2). For each slope, the number of evaluated data points is given in brackets

Re_1^*	$M = 0.35$	$M = 0.50$	$M = 0.65$
17.5			
22.5		−23.33 (5)	
30.0			−26.92 (2)
40.0			−44.74 (2)
50.0	−45.51 (2)		−50.71 (3)
60.0			−60.92 (2)
70.0			−58.99 (2)
80.0			−62.53 (2)

Table 8 Slopes, $h_{II,1}$, of configuration with $h = 20\,\mu m$ as a function of unit Reynolds number and Mach number (see Eq. 2). For each slope, the number of evaluated data points is given in brackets

Re_1^*	$M = 0.35$	$M = 0.50$	$M = 0.65$
17.5			
22.5		−19.85 (5)	
30.0	−22.18 (3)	−23.83 (2)	−20.82 (5)
40.0	−29.26 (3)	−31.06 (2)	−22.42 (2)
50.0	−33.63 (3)	−31.51 (3)	−31.26 (4)
60.0			−28.63 (2)
70.0			−33.92 (3)
80.0			−36.46 (2)

Table 9 Slopes, $h_{II,1}$, of configuration with $h = 30\,\mu m$ as a function of unit Reynolds number and Mach number (see Eq. 2). For each slope, the number of evaluated data points is given in brackets

Re_1^*	$M = 0.35$	$M = 0.50$	$M = 0.65$
17.5	−13.30 (5)		
22.5		−15.14 (5)	
30.0	−21.33 (5)	−19.80 (7)	−18.07 (7)
40.0	−25.23 (2)	−25.76 (2)	−21.43 (4)
50.0	−27.11 (3)	−24.13 (2)	−22.82 (3)
60.0			−24.95 (2)
70.0			−27.77 (2)
80.0			−29.92 (3)

Table 10 Slopes, $h_{II,1}$, of configuration with $h = 40\,\mu m$ as a function of unit Reynolds number and Mach number (see Eq. 2). For each slope, the number of evaluated data points is given in brackets

Re_1^*	$M = 0.35$	$M = 0.50$	$M = 0.65$
17.5	−11.92 (5)		
22.5		−14.14 (5)	
30.0	−20.32 (7)	−17.35 (5)	−12.63 (13)
40.0	−20.97 (4)	−18.94 (5)	−13.99 (3)
50.0	−18.93 (6)		
60.0			
70.0			
80.0			

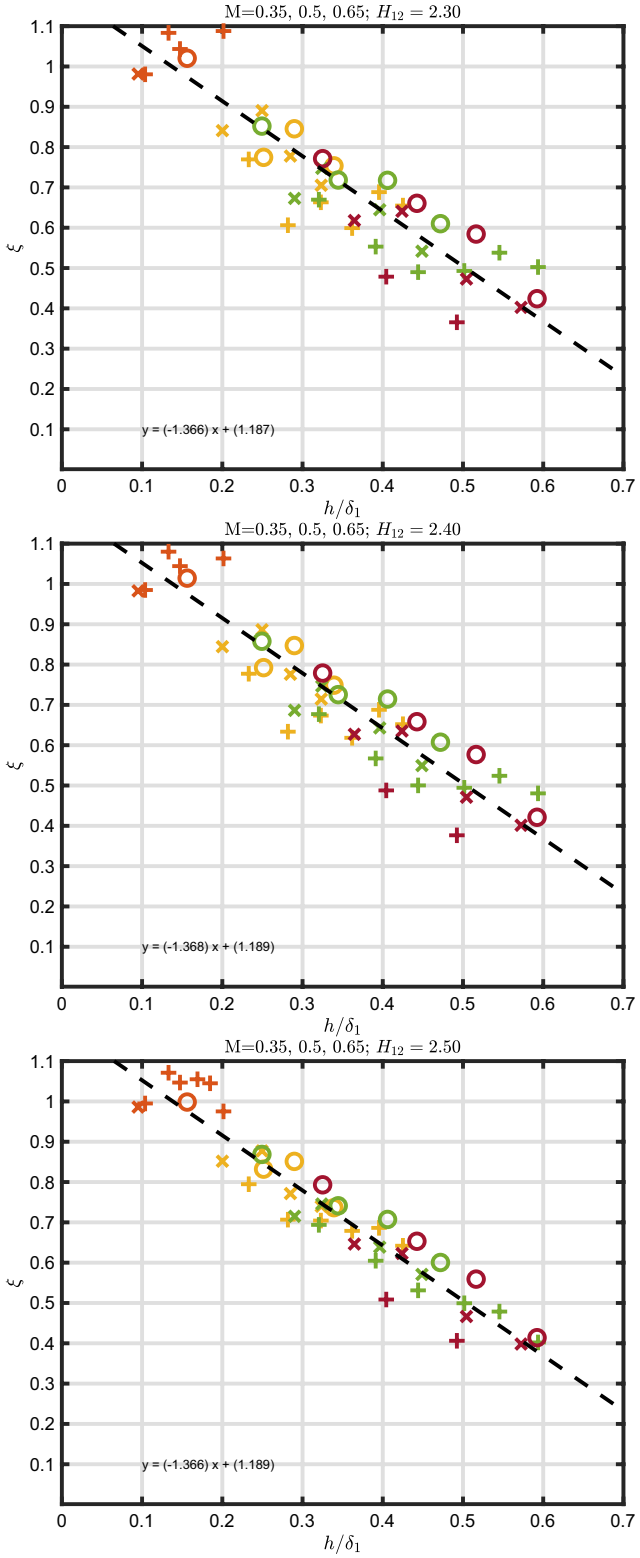

Fig. 58 The parameter ξ as a function of normalized step height h/δ_1 for all Mach numbers and configurations with $H_{12} = 2.30$, 2.40 and 2.50 . The legend for all data points is shown separately in Fig. 5

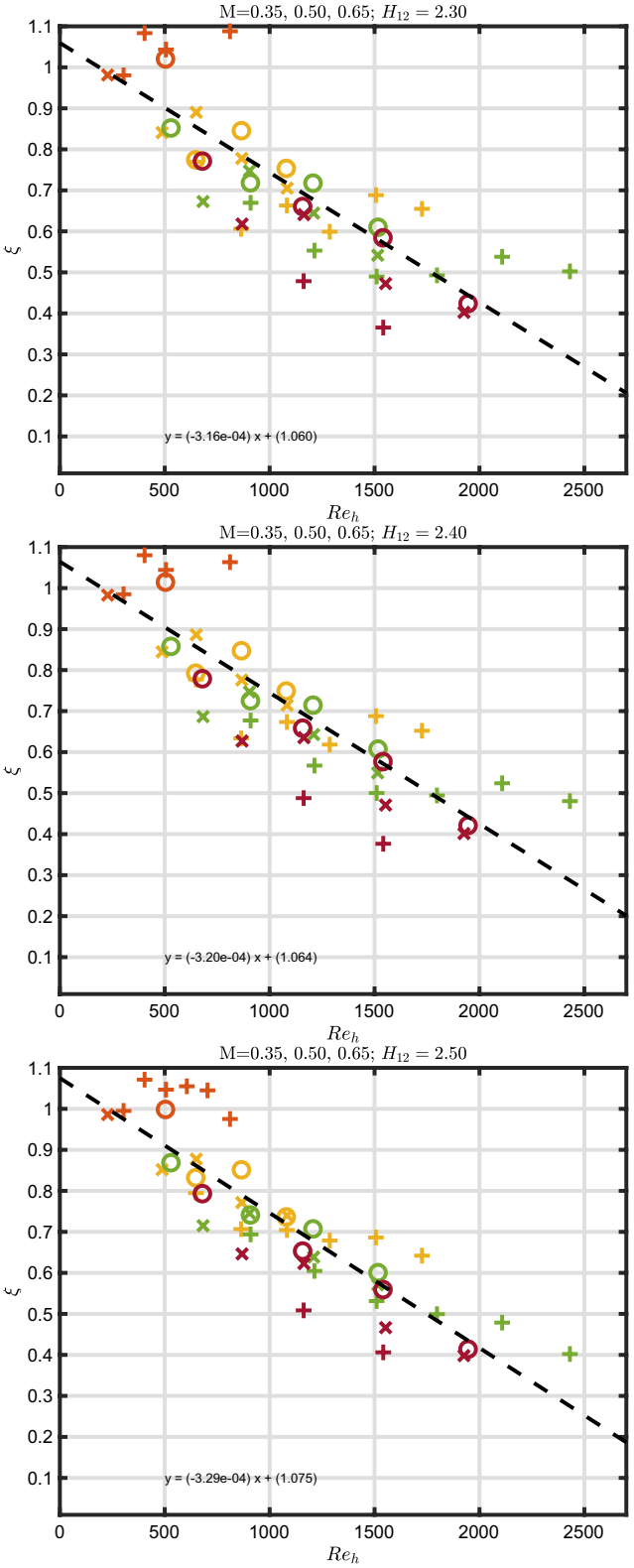

Fig. 59 The parameter ξ as a function of step-height Reynolds number Re_h for all Mach numbers and configurations with $H_{12} = 2.30$, 2.40 and 2.50 (from top to bottom). The legend is shown separately in Fig. 5

Details of the transition Reynolds number analysis

The approximated linear functions described above can be used to calculate the transition Reynolds numbers at specific shape factors. The results are shown for $H_{12} = 2.55$ in Fig. 56 with its corresponding legend in Fig. 5. The black symbols represent the transition Reynolds numbers measured with the reference configuration. The orange, yellow, green and dark-red symbols indicate the transition Reynolds numbers measured with step heights of 10 µm, 20 µm, 30 µm and 40 µm, respectively. For comparison, the purple dots mark the flow length Reynolds number of the step location at $x_S/c = 0.35$. The transition Reynolds numbers for other calculated shape factors $H_{12} = 2.30$, 2.40 and 2.50 are shown in Fig. 57. It should be stressed here that they were not measured directly but calculated based on the linear approximations. This approach is very helpful to understand general trends, as presented in the following.

It can be seen from Fig. 57 that the variation of $\mathrm{Re}^*_{\mathrm{tr}}$ as a function of Re_1 is larger at smaller H_{12}. This effect is caused by the stronger acceleration of the boundary layer. It results in a weaker amplification of the T-S waves at smaller H_{12}, which can be observed by comparing the gradients of the N-factor curves (Risius et al. 2023). A stronger pressure gradient reduces the slope of the N-factor curves and results in a larger difference between the transition locations. This so-called sensitivity effect has been described before in detail for forward-facing steps in Costantini et al. (2015b, 2016); Costantini (2016).

The overview graphs in Fig. 56 also show a reduction of the transition Reynolds numbers by installation of the steps. It should be noted here that the extrapolation of the results for very small shape factors ($H_{12} = 2.30$) and large unit Reynolds numbers ($\mathrm{Re}^*_1 = 60$ to 80) leads to a large uncertainty in the calculation of the transition Reynolds number $\mathrm{Re}^*_{\mathrm{tr}}$. That may result in the misleading observation of the 10 µm step configuration exhibiting a significantly larger transition Reynolds number than the reference configuration. However, this observation must rather be interpreted as an increased uncertainty due to the large extrapolation range.

Details of shape factor H_{12} and pressure gradient influences

Thanks to the systematic variation of the pressure gradient and the linear approximation of the results, the present study allows to investigate ξ for different values of the shape factor H_{12}. A comparison of the ξ parameter for different H_{12} is shown in Fig. 58 (as a function of h/δ_1) and in Fig. 59 (as a function of Re_h). It can be seen that the values of the linear approximation m and b are very similar for different shape factors $H_{12} = 2.30$, 2.40 , 2.50 and 2.55 (Table 2).

A clear trend cannot be observed when the ξ parameter is plotted as a function of h/δ_1 for different H_{12} (Fig. 58). However, a slight increase of ξ with H_{12} can be seen, when ξ is investigated as a function of Re_h (see Fig. 59 and Table 2). Within the measurement accuracy, these results are in agreement with earlier results for forward-facing steps (Costantini et al. 2022) and with results for gaps (Risius et al. 2023), where a small systematic influence of the shape factor on ξ was detected.

It is interesting to note that the values for slope and intercept remain similar for different H_{12} (see Table 2), while the scattering of the data points decreases with increasing H_{12} (see Figs. 58 and 59). This trend can be explained by the larger amount of measurement data at larger H_{12} leading to a smaller uncertainty.

The shown N-factor distributions exhibit a plateau for decelerated boundary layers with $H_{12} \gtrsim 2.59$ (see Fig. 7). For accelerated and neutral boundary layers with $H_{12} \lesssim 2.59$, where the pressure gradient is close to zero, the transition N-factors decrease almost linearly with shape factor H_{12}. This finding is in agreement with the results reported in Risius et al. (2018b, 2023). It is shown in Fig. 7 and in the bottom figures in Appendix (Figs. 16, 19, 22, 25, 28, 31, 34, 37, 40, 43, 46, 49, 52) that the influence of the pressure gradient on the transition N-factors is similar for all BFS configurations as on the reference configuration for $H_{12} \lesssim 2.59$.

Details of unit Reynolds number influence

The influence of the unit Reynolds number, Re_1, on the transition Reynolds number, $\mathrm{Re}_{\mathrm{tr}}$, and the transition N-factor is reported in detail in Risius et al. (2018b) for the reference configuration and in Risius et al. (2023) for the gap configuration. The general trend of an increasing $\mathrm{Re}_{\mathrm{tr}}$ with increasing Re_1 was also found in the current investigation of backward-facing steps (see Figs. 8 and 56, 57).

Details of Mach number influence on the N-factor

The Mach number M shows no systematic influence on the relative reduction of the transition N-factor, at least in the examined Mach number range (Fig. 53). This result is in line with the findings reported in Sect. 1, in which no appreciable influence of the Mach number on transition Reynolds number and on ξ was observed. It is also in agreement with the results reported earlier for gap configurations (Risius et al. 2023).

Details of step-height influences

As expected, in general increasing normalized step height h/δ_1 and step-height Reynolds number Re_h lead to an increasing reduction of the laminar flow length, corresponding to a smaller Re_{tr} (Fig. 56). However, the results (Figs. 3 and 4) also show that this observation is only true for backward-facing steps with $h > 10\,\mu\mathrm{m}$. These observations are consistent for all investigated Mach and Reynolds numbers, as shown in the middle figures in Appendix (Figs. 15, 18, 21, 24, 27, 30, 33, 36, 39, 42, 45, 48, 51).

Repeatability of wind tunnel entries and flow quality

As described in Sect. 2.3 and Risius et al. (2018b, 2023), the measurements were conducted over a time span of two years in six different measurement campaigns. During this period, the model was reassembled several times and the reference configuration was repeatedly tested in each wind tunnel entry. The good repeatability of the data can be seen by comparing the reference data of different measurement campaigns (Figs. 13, 14, 17, 20, 23, 26, 29, 32, 35, 38, 41). The same good repeatability was observed for the configuration with gaps (Risius et al. 2023).

The total temperature turbulence level, Tu_{T_0}, in the center of the test section, is lower than 0.04 % at Mach number $M = 0.8$, unit Reynolds number $\mathrm{Re}_1 = 30 \times 10^6\,\mathrm{m}^{-1}$ and charge temperature $T_c \approx 282\,\mathrm{K}$, and it decreases with lower Mach numbers[2]. The mass flux turbulence level[2], $Tu_{\rho u}$, in the center of the test section is approximately 0.06% at $M = 0.8$, $T_c \approx 283\,\mathrm{K}$ and $30 \times 10^6 < \mathrm{Re}_1 < 77 \times 10^6\,\mathrm{m}^{-1}$; it increases slightly at lower Mach numbers, but remains smaller than 0.08% (Koch 2004).

Uncertainties of measured parameters

The uncertainties of the measured parameters are similar to the ones discussed in Risius et al. (2018b, 2023). Uncertainties of the transition Reynolds number and of the pressure gradient parameter are in the range of $(Re^{\star}_{tr})_{\mathrm{RMS}} \approx 0.5$ and $(H_{12})_{\mathrm{RMS}} \approx 0.01$, which correspond to relative errors of about 5% and 0.5%, respectively. The maximal relative uncertainty of ξ can be estimated to be about 7%, which also corresponds to an absolute maximal error of $\Delta\xi \approx 0.07$.

In this context, it should be noted that the indirectly calculated values of $Re^{\star}_{tr}$ as shown in Figs. 56, 57 and 8 depend on the chosen value of H_{12}. For a value of H_{12} close to the measured data points, the extrapolation error is rather small, while it is larger, when a rather distant value of H_{12} is chosen.

The step height was measured with a profilometer at several instances along the span, and a detection of the steps sizes was carried out. From these instances, the mean and the standard deviation were calculated and found to be in the range of 5 µm.

The uncertainty of the derived parameter h/δ_1 can be estimated from Figs. 9, 11 and 58 to be in the range of $\Delta\left(h/\delta_1\right) \approx 0.05$. The variation of the step-height Reynolds number can be estimated from Figs. 10, 12 and 59 to be $\Delta\mathrm{Re}_h \approx 250$. By comparison with Figs. 58 and 59, it can be noted that the scattering of the data decreases with increasing shape factor. This observation can on the one hand be explained by the increasing amount of data points at larger H_{12} and on the other hand by the decreasing influence of the BFS on the transition locations with increasing H_{12} (Figs. 4, 15, 18, 21, 24, 27, 30, 33, 36, 39, 42, 45, 48, 51).

Summary of further datasets

The following datasets consist out of three parts. The first part shows the detailed results for each flow condition in a series of three succeeding images. The first image on top shows the transition Reynolds number of reference configuration at different wind tunnel entries (labeled as Reference 1–6). The individual results of the reference configurations are combined to give a linear reference function shown as dashed black lines in the top figures.

The second images in the middle show also the results of the reference configuration marked with black dashed lines. The purple dotted horizontal line marks the transition Reynolds number which corresponds to the location of the BFS at $x_S/c = 0.35$ with $\mathrm{Re}_{x_S} = x_S \cdot \mathrm{Re}_1$. In the middle between the boundaries given by the reference configuration and the BFS location, the measured transition Reynolds numbers of different BFS configurations are shown by orange ($h = 10\,\mu\mathrm{m}$), yellow ($h = 20\,\mu\mathrm{m}$), green ($h = 30\,\mu\mathrm{m}$) and red ($h = 40\,\mu\mathrm{m}$) lines.

The last image at the bottom shows the corresponding results of the transition N-factors. In the ranges of H_{12} where a linear increase in the transition N-factor was observed, a linear function with an average slope was fitted to the results. The offset between the different linear approximations was used to determine the value of ΔN used for the analysis in Sect. 3.5.

The second part of Appendix contains Figs. 53, 54, 55, 56 and 57 as well as Tables 3, 4, 5, 6, 7, 8, 9 and 10 of the fitted linear approximations with intercepts, $h_{II,0}$, and slopes, $h_{II,1}$, of Eq. 2 for each BFS configuration. Following the analysis of Risius et al. (2018b) and Risius et al. (2023), it was found that the transition Reynolds number increases almost

[2] The turbulence level of a quantity x is defined as $Tu_x = \sqrt{\overline{(x-\bar{x})^2}}/\bar{x} = x_{\mathrm{RMS}}/\bar{x}$, where $\bar{x}$ is the temporal average of x and x_{RMS} is the RMS of the fluctuations.

linearly with a more pronounced favorable pressure gradient, corresponding to a shape factor decrease, as shown in Fig. 13 for $M = 0.5$ and $\mathrm{Re}_1^* = 22.5$ (chord Reynolds number $\mathrm{Re}_c = 4.5 \times 10^6$.). Consequently, a linear function

$$\mathrm{Re}_{\mathrm{tr}}^* = h_{II,1} \cdot H_{12} + h_{II,0} \tag{2}$$

with an intercept, $h_{II,0}$, and a slope, $h_{II,1}$, was fitted through the data for each combination of Mach and Reynolds number (shown by solid lines of the corresponding colors in Fig. 13).[3] Average slopes and intercepts were then calculated, and the fitted functions are shown as dashed lines in the corresponding figures. The measurement uncertainty of $\mathrm{Re}_{\mathrm{tr}}^*$ is in the range of the symbol size or below. The average coefficients $h_{II,0}$ and $h_{II,1}$ are summarized for all cases in Risius et al. (2023).

In general, it was also found for the configuration with BFS that an increasing unit Reynolds number leads to an increasing transition Reynolds number (Fig. 54 and Tables 3, 4, 5 and 6) and an increasing unit Reynolds number leads to a decreasing slope (Fig. 55 and Tables 7, 8, 9 and 10).

Exceptions from these general trends may be accounted to the limited measurement accuracy. Furthermore, the basis for this extrapolation at high Mach and Reynolds numbers are only a few data points. However, it should be stressed that the observed scattering of the intercept for different Mach numbers at $\mathrm{Re}_{\mathrm{tr}}^\star = 30$, 40 and 50 is approximately $\Delta\mathrm{Re}_{\mathrm{tr}}^\star \approx 20$ and based on a significant extrapolation of the measurement data.

The third part of Appendix shows a comparison of the ξ parameter for different H_{12} in Fig. 58 as a function of h/δ_1 and in Fig. 59 as a function of Re_h. This comparison is made possible by the systematic variation of the pressure gradient and the linear approximation of the results. As already stated, the scattering of the data decreases with increasing shape factor, which can on the one hand be explained by the increasing amount of data points at larger H_{12} and on the other hand by the decreasing influence of the BFS on the transition locations with increasing H_{12}.

Acknowledgements We would like to thank C. Klein (DLR) for TSP application and his continuous, invaluable assistance and backing of these investigations; A. Dillmann, L. Koop, M. Rein, H. Rosemann (all DLR) for their support and advise; U. G. Becker (DLR), C. Fuchs (DLR), T. Kleindienst (DLR), V. Ondrus (FH Münster) and L. Schojda (previously DLR) for model and test preparation; and W. H. Beck, B. D. Dimond, S. Hein, U. Henne, M. Hilfer, S. Koch, J. Lemarechal, A. Weiss (all DLR) and W. E. Sachs (previously DLR) for their help during the measurement campaign, data evaluation and interpretation. Furthermore, we would like to thank M. Aschoff (DLR), S. Hucke and R. Kahle (previously DLR) for the support during the wind tunnel test campaigns. We also thank two anonymous referees for their helpful comments.

[3] The labeling of the function and parameters corresponds to nomenclature of Risius et al. (2018b) on which the following analysis is based. It is kept identical for consistency and transparency, although the variable h is used for the step height in this work.

Author contributions Both authors contributed to the study conception and design. Material preparation, data collection and analysis were performed by Steffen Risius. The first draft of the manuscript was written by Steffen Risius, and both authors commented on previous versions of the manuscript. Both authors read and approved the final manuscript.

Funding Open Access funding enabled and organized by Projekt DEAL. No funding was received to assist with the preparation of this manuscript.

Data availability The datasets generated and analyzed during the current study are available from the corresponding author upon reasonable request and with permission of the German Aerospace Center (DLR).

Declarations

Ethical approval Not applicable.

Conflict of interest The authors have no conflict of interest to declare that are relevant to the content of this article.

References

Al-Maaitah AA, Nayfeh AH, Ragab SA (1990) Effect of suction on the stability of subsonic flows over smooth backward-facing steps. AIAA J 28(11):1916–1924. https://doi.org/10.2514/3.10499

Al-Maaitah AA, Nayfeh AH, Ragab SA (1990) Effect of wall cooling on the stability of compressible subsonic flows over smooth humps and backward-facing steps. Phys Fluids A 2(3):381–389. https://doi.org/10.1063/1.857788

Arnal D (1989) Laminar-turbulent transition problems in supersonic and hypersonic flows. In: AGARD Special Course on Aerothermodynamics of Hypersonic Vehicles, AGARD-R-761, AGARD, Advisory Group for Aerospace Research and Development, Rhode-Saint-Genèse, Belgium, pp 8–1–8–45

Arnal D (1992) Boundary layer transition: Prediction, application to drag reduction. Tech. Rep. AGARD Rept. 786, Advidsory Group for Aerospace Research and Development

Arnal D, Casalis G, Cousteix J, Reneaux J (1997) Laminar-turbulent transition in subsonic boundary layers - Research and applications in France. In: 28th Fluid Dynamics Conference. American Institute of Aeronautics and Astronautics. https://doi.org/10.2514/6.1997-1905

Beguet S, Perraud J, Forte M, Brazier JP (2017) Modeling of transverse gaps effects on boundary-layer transition. J Aircr 54(2):794–801. https://doi.org/10.2514/1.C033647

Costantini M (2016) Experimental analysis of geometric, pressure gradient and surface temperature effects on boundary-layer transition in compressible high Reynolds number flow. PhD thesis, RWTH Aachen University, Aachen

Costantini M, Fey U, Henne U, Klein C (2015) Nonadiabatic surface effects on transition measurements using temperature-sensitive paints. AIAA J 53(5):1172–1187. https://doi.org/10.2514/1.J053155

Costantini M, Risius S, Klein C (2015) Experimental investigation of the effect of forward-facing steps on boundary layer transition. Procedia IUTAM 14:152–162. https://doi.org/10.1016/j.piutam.2015.03.036

Costantini M, Risius S, Klein C, Kühn W (2016) Effect of forward-facing steps on boundary layer transition at a subsonic Mach number. In: New Results in Numerical and Experimental Fluid Mechanics X, Notes on Numerical Fluid Mechanics and Multidisciplinary Design, Springer, Cham, pp 203–213, https://doi.org/10.1007/978-3-319-27279-5_18

Costantini M, Risius S, Klein C (2018) Non-adiabatic surface effects on step-induced boundary-layer transition. Flow Turbul Combust 100(4):1145–1177. https://doi.org/10.1007/s10494-018-9913-7

Costantini M, Henne U, Risius S, Klein C (2021) A robust method for reliable transition detection in temperature-sensitive paint data. Aerosp Sci Technol 113:106702. https://doi.org/10.1016/j.ast.2021.106702

Costantini M, Risius S, Klein C (2022) Step-induced transition in compressible high Reynolds number flow. Flow 2:E33. https://doi.org/10.1017/flo.2022.21

Crouch J, Kosorygin V, Ng L (2006) Modeling the effects of steps on boundary-layer transition. In: Govindarajan R (ed) IUTAM Symposium on Laminar-Turbulent Transition, Springer Netherlands, Dordrecht, Fluid Mechanics and Its Applications, pp 37–44, https://doi.org/10.1007/1-4020-4159-4_4

Crouch JD (2022) Predicting Laminar-Turbulent Transition Influenced by Surface-Induced Flow Distortions. In: Sherwin S, Schmid P, Wu X (eds) IUTAM Laminar-Turbulent Transition, Springer International Publishing, Cham, IUTAM Bookseries, pp 19–32, https://doi.org/10.1007/978-3-030-67902-6_2

Crouch JD, Kosorygin VS (2020) Surface step effects on boundary-layer transition dominated by Tollmien-Schlichting instability. AIAA J 58(7):2943–2950. https://doi.org/10.2514/1.J058518

Crouch JD, Kosorygin VS, Sutanto MI, Miller GD (2022) Characterizing surface-gap effects on boundary-layer transition dominated by Tollmien-Schlichting instability. Flow 2:E8. https://doi.org/10.1017/flo.2022.1

Dimond B, Costantini M, Risius S, Fuchs C, Klein C (2019) Experimental analysis of suction on step-induced boundary-layer transition. Exp Thermal Fluid Sci 109(109):842. https://doi.org/10.1016/j.expthermflusci.2019.109842

Dimond B, Costantini M, Risius S, Klein C, Rein M (2020) Experimental Investigation of the Delay of Gap- and Step-Induced Transition by Means of Suction. In: Dillmann A, Heller G, Krämer E, Wagner C, Tropea C, Jakirlić S (eds) New Results in Numerical and Experimental Fluid Mechanics XII, Springer International Publishing, Cham, Notes on Numerical Fluid Mechanics and Multidisciplinary Design, pp 165–174, https://doi.org/10.1007/978-3-030-25253-3_16

Dimond B, Costantini M, Klein C (2021) Experimental Analysis of the Effect of Suction and Step Height on Boundary-Layer Transition. In: Sherwin S, Schmid P, Wu X (eds) IUTAM Laminar-Turbulent Transition, Springer International Publishing, Cham, IUTAM Bookseries, pp 171–180, https://doi.org/10.1007/978-3-030-67902-6_14

Drake A, Bender A, Korntheuer A, Westphal R, Rohe W, Dale G, McKeon B, Geraschchenko S (2010) Step Excrescence Effects for Manufacturing Tolerances on Laminar Flow Wings. In: 48th AIAA Aerospace Sciences Meeting Including the New Horizons Forum and Aerospace Exposition. American Institute of Aeronautics and Astronautics. https://doi.org/10.2514/6.2010-375

Dryden HL (1953) Review of published data on the effect of roughness on transition from laminar to turbulent flow. J Aeronaut Sci 20(7):477–482. https://doi.org/10.2514/8.2693

Duncan GT, Crawford B, Tufts MW, Saric WS, Reed HL (2013) Effects of Step Excrescences on Swept-Wing Transition. In: 31st AIAA Applied Aerodynamics Conference. American Institute of Aeronautics and Astronautics. https://doi.org/10.2514/6.2013-2412

EASA (2017) Type-Certificate Data Sheet No. EASA.A.064 - Airbus A318, A319, A320, A321

EASA (2023) Type-Certificate Data Sheet No. EASA.IM.A.120 - Boeing 737

Edelmann CA, Rist U (2015) Impact of forward-facing steps on laminar-turbulent transition in transonic flows. AIAA J 53(9):2504–2511. https://doi.org/10.2514/1.J053529

Egami Y, Fey U, Klein C, Quest J, Ondrus V, Beifuss U (2012) Development of new two-component temperature-sensitive paint (TSP) for cryogenic testing. Measur Sci Technol 23(11):115301. https://doi.org/10.1088/0957-0233/23/11/115301

Eppink JL, Wlezien RW, King RA, Choudhari M (2018) Interaction of a backward-facing step and crossflow instabilities in boundary-layer transition. AIAA J 56(2):497–509. https://doi.org/10.2514/1.J056267

Franco JA, Hein S (2022) Numerical Studies on the Influence of Step-Like Surface Irregularities on the Development of Tollmien-Schlichting Waves. In: Sherwin S, Schmid P, Wu X (eds) IUTAM Laminar-Turbulent Transition, Springer International Publishing, Cham, pp 737–748, https://doi.org/10.1007/978-3-030-67902-6_64

Franco JA, Theiss A, Hein S (2021) Influence of Surface Irregularities on the Expected Boundary-Layer Transition Location on Hybrid Laminar Flow Control Wings. In: Dillmann A, Heller G, Krämer E, Wagner C (eds) New Results in Numerical and Experimental Fluid Mechanics XIII, Springer International Publishing, Cham, pp 174–184, https://doi.org/10.1007/978-3-030-79561-0_17

Hahn M, Pfenninger W (1973) Prevention of transition over a backward step by suction. J Aircr 10(10):618–622. https://doi.org/10.2514/3.60269

Heintz A, Scholz P (2023) Measurements on the effect of steps on the transition of laminar boundary layers. Exp Fluids 64(4):76. https://doi.org/10.1007/s00348-023-03614-x

Hildebrand N, Choudhari MM, Paredes P (2020) Predicting boundary-layer transition over backward-facing steps via linear stability analysis. AIAA J 58(9):3728–3734. https://doi.org/10.2514/1.J059713

Holmes BJ, Obara CJ, Martin GL, Domack CS (1985) Manufacturing Tolerances for Natural Laminar Flow Airframe Surfaces. SAE Technical Paper 850863, SAE International, Warrendale, PA, https://doi.org/10.4271/850863

Koch S (2004) Zeitliche und räumliche Turbulenzentwicklung in einem Rohrwindkanal und deren Einfluss auf die Transition an Profilmodellen. PhD thesis, Georg-August-University, Göttingen

Liu T, Sullivan JP, Asai K, Klein C, Egami Y (2021) Pressure and Temperature Sensitive Paints, 2nd edn. Springer, Berlin

Masad JA, Nayfeh AH (1993) The Influence of Imperfections on the Stability of Subsonic Boundary Layers. In: Ashpis DE, Gatski

TB, Hirsh R (eds) Instabilities and Turbulence in Engineering Flows, Springer Netherlands, Dordrecht, pp 65–82, https://doi.org/10.1007/978-94-011-1743-2_4

Nenni JP, Gluyas GL (1966) Aerodynamic design and analysis of an LFC surface. Astronaut Aeronaut 4(7):52–57

Ondrus V, Meier RJ, Klein C, Henne U, Schäferling M, Beifuss U (2015) Europium 1,3-di(thienyl)propane-1,3-diones with outstanding properties for temperature sensing. Sens Actuators, A 233:434–441. https://doi.org/10.1016/j.sna.2015.07.023

Özçakmak ÖS, Madsen HA, Sørensen NN, Sørensen JN (2020) Laminar-turbulent transition characteristics of a 3-D wind turbine rotor blade based on experiments and computations. Wind Energy Sci 5(4):1487–1505. https://doi.org/10.5194/wes-5-1487-2020

Perraud J, Séraudie A (2000) Effects of Steps and Gaps on 2D and 3D Transition. In: European Congress on Computational Methods in Applied Sciences and Engineering

Ragab SA, Nayfeh AH, Krishna RC (1989) Stability of compressible boundary layers over a smooth backward-facing step. Tech. Rep. NR-4325201, Department of Engineering Science and Mechanics Virginia Polytechnic Institute and State University Blacksburg, Virginia

Risius S (2018) Development of a time-resolved quantitative surface-temperature measurement technique and its application in short-duration wind tunnel testing. PhD thesis, Georg-August-University Göttingen

Risius S, Costantini M, Hein S, Koch S, Klein C (2018a) Experimental investigation of Mach number and pressure gradient effects on boundary layer transition in two-dimensional flow. In: New Results in Numerical and Experimental Fluid Mechanics XI, Notes on Numerical Fluid Mechanics and Multidisciplinary Design, Springer, Cham, pp 305–314, https://doi.org/10.1007/978-3-319-64519-3_28

Risius S, Costantini M, Koch S, Hein S, Klein C (2018b) Unit Reynolds number, Mach number and pressure gradient effects on laminar-turbulent transition in two-dimensional boundary layers. Exp Fluids. https://doi.org/10.1007/s00348-018-2538-8

Risius S, Costantini M, Klein C (2023) Influence of deep gaps on laminar-turbulent transition in two-dimensional boundary layers at subsonic Mach numbers. Exp Fluids 64(11):174. https://doi.org/10.1007/s00348-023-03708-6

Rius-Vidales AF, Kotsonis M (2021) Impact of a forward-facing step on the development of crossflow instability. J Fluid Mech 924:A34. https://doi.org/10.1017/jfm.2021.497

Rizzetta DP, Visbal MR (2013) The Effect of Two-Dimensional Geometric Disturbances on Boundary-Layer Stability. In: 43rd AIAA Fluid Dynamics Conference. American Institute of Aeronautics and Astronautics, San Diego, CA. https://doi.org/10.2514/6.2013-3108

Rosemann H (1997) The Cryogenic Ludwieg-Tube Tunnel at Göttingen. In: Special Course on Advances in Cryogenic Wind Tunnel Technology, AGARD R-812, Neuilly-sur-Seine, pp 8–1–8–13

Schlichting H, Gersten K (2006) Grenzschicht-Theorie, 10th edn. Springer, Berlin

Schrauf G (1998) COCO-A program to compute velocity and temperature profiles for local and nonlocal stability analysis of compressible, conical boundary layers with suction. ZARM Technik report

Schrauf G (2005) Status and perspectives of laminar flow. Aeronaut J 109(1102):639–644. https://doi.org/10.1017/S000192400000097X

Schrauf G (2006) LILO 2.1 User's guide and tutorial. Bremen, Germany, GSSC Technical Report 6

Schrauf G (2018) On Allowable Step Heights:Lessons Learned from the F100 and ATTAS Flight Tests. In: 6th European Conference on Computational Mechanics (ECCM6) and 7th European Conference on Computational Fluid Mechanics (ECFD7), Glasgow

Schröder A, Schanz D, Heine B, Dierksheide U (2013) Investigation of Transitional Flow Structures Downstream of a Backward-Facing-Step by Using 2D–2C- and High Resolution 3D–3C-Tomo- PIV. In: Dillmann A, Heller G, Kreplin HP, Nitsche W, Peltzer I (eds) New Results in Numerical and Experimental Fluid Mechanics VIII, vol 121. Springer, Berlin, pp 219–226. https://doi.org/10.1007/978-3-642-35680-3_27

Smith AMO, Clutter DW (1959) The smallest height of roughness capable of affecting boundary-layer transition. J Aerosp Sci 26(4):229–245. https://doi.org/10.2514/8.8019

Smith AMO, Gamberoni N (1956) Transition, pressure gradient, and stability theory. Tech. Rep. ES. 26388, Douglas Aircraft Co Inc, El Segundo, CA

Tani I (1961) Effect of two-dimensional and isolated roughness on laminar flow. In: Boundary Layer and Flow Control, Elsevier, pp 637–656, https://doi.org/10.1016/B978-1-4832-1323-1.50004-X

Tocci F, Chauvat G, Hein S, Hanifi A (2022) Direct Numerical Simulations of Tollmien-Schlichting Disturbances in the Presence of Surface Irregularities. In: Sherwin S, Schmid P, Wu X (eds) IUTAM Laminar-Turbulent Transition, Springer International Publishing, Cham, pp 805–814, https://doi.org/10.1007/978-3-030-67902-6_70

Tufts MW, Reed HL, Crawford BK, Duncan GT, Saric WS (2017) Computational investigation of step excrescence sensitivity in a swept-wing boundary layer. J Aircr 54(2):602–626. https://doi.org/10.2514/1.C033892

van Ingen J (1956) A suggested semi-empirical method for the calculation of the boundary layer transition region. Tech. Rep. VTH-74, Technische Hogeschool Delft, Delft

Wang YX, Gaster M (2005) Effect of surface steps on boundary layer transition. Exp Fluids 39(4):679–686. https://doi.org/10.1007/s00348-005-1011-7

Zahn J, Rist U (2015) Impact of deep gaps on laminar-turbulent transition in compressible boundary-layer flow. AIAA J 54(1):66–76. https://doi.org/10.2514/1.J054112